The Astrophysical Journal, 997:61 (15pp), 2026 January 20 https://doi.org/10.3847/1538-4357/ae1eef

The Large-scale Environments of Low-luminosity AGNs at $3.9 < z < 6$ and Implications for Their Host Dark Matter Halos from a Complete NIRCam Grism Redshift Survey

Xiaojing Lin[1,2], Xiaohui Fan[2], Fengwu Sun[3], Junyu Zhang[2], Eiichi Egami[2], Jakob M. Helton[2], Feige Wang[4], Haowen Zhang[2], Andrew J. Bunker[5], Zheng Cai[1], Zhiyuan Ji[2], Xiangyu Jin[2], Roberto Maiolino[6,7,8], Maria Anne Pudoka[2], Pierluigi Rinaldi[2], Brant Robertson[9], Sandro Tacchella[6,10], Wei Leong Tee[2], Yang Sun[2], Christopher N. A. Willmer[2], Chris Willott[11], and Yongda Zhu[2]

[1] Department of Astronomy, Tsinghua University, Beijing 100084, People's Republic of China; xiaojinglin.astro@gmail.com
[2] Steward Observatory, University of Arizona, 933 N Cherry Avenue, Tucson, AZ 85721, USA
[3] Center for Astrophysics | Harvard & Smithsonian, 60 Garden Street, Cambridge, MA 02138, USA
[4] Department of Astronomy, University of Michigan, 1085 South University Avenue, Ann Arbor, MI 48109, USA
[5] Department of Physics, University of Oxford, Denys Wilkinson Building, Keble Road, Oxford OX13RH, UK
[6] Kavli Institute for Cosmology, University of Cambridge, Madingley Road, Cambridge, CB3 0HA, UK
[7] Cavendish Laboratory—Astrophysics Group, University of Cambridge, 19 JJ Thomson Avenue, Cambridge, CB3 0HE, UK
[8] Department of Physics and Astronomy, University College London, Gower Street, London WC1E 6BT, UK
[9] Department of Astronomy and Astrophysics, University of California, Santa Cruz, 1156 High Street, Santa Cruz, CA 95064, USA
[10] Cavendish Laboratory, University of Cambridge, 19 JJ Thomson Avenue, Cambridge, CB3 0HE, UK
[11] NRC Herzberg, 5071 West Saanich Road, Victoria, BC V9E 2E7, Canada
Received 2025 May 5; revised 2025 November 2; accepted 2025 November 10; published 2026 January 14

Abstract

We study the large-scale environments and clustering properties of 28 low-luminosity active galactic nuclei (AGNs) at $z = 3.9$–6 in the GOODS-N field. Our sample, identified from the JWST NIRCam Imaging and WFSS data in Complete NIRCam Grism Redshift Survey and First Reionization Epoch Spectroscopically Complete Observations surveys with either broad Hα emission lines or V-shaped continua, are compared to 782 Hα emitters (HAEs) selected from the same data. These AGNs are located in diverse large-scale environments and do not preferentially reside in denser environments compared to HAEs. Their overdensity field, δ, averaged over $(15\,h^{-1}\,\mathrm{cMpc})^3$, ranges from -0.56 to 10.56, and shows no clear correlation with broad-line luminosity, black hole (BH) masses, or the AGN fraction. It suggests that >10 cMpc structures do not significantly influence BH growth. We measure the two-point cross-correlation function of AGNs with HAEs, finding a comparable amplitude to that of the HAE autocorrelation. This indicates similar bias parameters and host dark matter halo masses for AGNs and HAEs. The correlation length of field AGNs is $4.26\,h^{-1}$ cMpc and $7.66\ h^{-1}$ cMpc at $3.9 < z < 5$ and $5 < z < 6$, respectively. We infer a median host dark matter halo mass of $\log(M_h/M_\odot) \approx 11.0 - 11.2$ and host stellar masses of $\log(M_\star/M_\odot) \approx 8.4 - 8.6$ by comparing with the UniverseMachine simulation. Our clustering analysis suggests that low-luminosity AGNs at high redshift reside in normal star-forming galaxies with overmassive BHs. They represent an intrinsically distinct population from luminous quasars and could be a common phase in galaxy evolution.

Unified Astronomy Thesaurus concepts: Supermassive black holes (1663); Clustering (1908); Galaxy dark matter halos (1880); Active galactic nuclei (16); Low-luminosity active galactic nuclei (2033); James Webb Space Telescope (2291)

1. Introduction

Over the past few decades, the discovery of UV-luminous quasars at $z \gtrsim 6$ has reshaped and challenged our understanding of supermassive black holes (SMBHs) in the early Universe (e.g., E. Bañados et al. 2018; J. Yang et al. 2020; F. Wang et al. 2021; X. Fan et al. 2023). These $z > 6$ quasars, hosting SMBHs exceeding $10^9\,M_\odot$ (e.g., J. Yang et al. 2021; E. P. Farina et al. 2022), have motivated extensive work on models of BH growth modes and seeding mechanisms (e.g., K. Inayoshi et al. 2022; V. Cammelli et al. 2024; J. Regan & M. Volonteri 2024). Multiple approaches have been proposed to constrain quasar lifetimes and duty cycles, including studies of quasars' proximity zones (A.-C. Eilers et al. 2017; F. B. Davies et al. 2020; A.-C. Eilers et al. 2020), damping wing features (F. B. Davies et al. 2019; J. F. Hennawi et al. 2024), and clustering properties (A.-C. Eilers et al. 2024; E. Pizzati et al. 2024). These independent approaches suggest quasar lifetimes of $\sim 10^6$ yr, with low duty cycles ($\ll 1$). These findings imply a very short timescale for quasar accretion and extremely rapid BH growth with low radiative efficiency ($\lesssim 0.1\%$; F. B. Davies et al. 2019; A.-C. Eilers et al. 2024). Alternatively, the bulk of SMBH growth history might have been enshrouded by dust and thus missed by current surveys (A. Comastri et al. 2015; Y. Ni et al. 2020; E. Lambrides et al. 2024a). The demographics of a broader BH population is the key to understanding the early BH assembly history.

The unprecedented near-infrared capabilities of the James Webb Space Telescope (JWST; J. P. Gardner et al. 2023) have brought new insights. Since its launch, JWST has revealed new populations of low-luminosity active galactic nuclei (AGNs) at $z > 4$, many of which are nicknamed as "little red dots" due to their compact morphology and unique spectral energy distributions (SEDs) in the near-IR wavelengths (e.g.,

H. B. Akins et al. 2024; J. E. Greene et al. 2024; V. Kokorev et al. 2024; X. Lin et al. 2024; J. Matthee et al. 2024; P. G. Pérez-González et al. 2024; P. Rinaldi et al. 2024). They often exhibit broad Balmer emission lines with FWHM exceeding 1000 km s^{-1}. Assuming these broad emission lines originate from the AGN broad-line region, they suggest SMBHs with masses ranging from $10^6 M_\odot$ to $\lesssim 10^9 M_\odot$ (e.g., J. E. Greene et al. 2024; X. Lin et al. 2024). While JWST has revealed these previously unseen objects, their nature and connection to UV-luminous quasars remain elusive. For instance, there is an ongoing debate regarding the origin of the so-called "V-shaped" continua observed in many of these objects, which exhibit a reddened rest-frame optical continuum and a bluer UV continuum slope (e.g., Z. Li et al. 2024; Y. Ma et al. 2024). It is also difficult to explain the absence of a hot dust torus (C. M. Casey et al. 2024; P. G. Pérez-González et al. 2024; C. C. Williams et al. 2024), the weakness of X-rays (R. Maiolino et al. 2024; M. Yue et al. 2024a), and the lack of variability in both UV and optical bands (M. Kokubo & Y. Harikane 2025; W. L. Tee et al. 2024; Z. Zhang et al. 2024), which are typical features of UV-luminous quasars. The high spatial resolution of NIRCam short-wavelength imaging reveals that ∼30% of LRDs exhibit signs of interaction, suggesting a potential link to merger-driven activities (P. Rinaldi et al. 2024). Some theoretical hypotheses propose that the broad emission lines may not originate from SMBHs, but rather from unusual galaxy kinematics or outflows (J. F. W. Baggen et al. 2024; M. Kokubo & Y. Harikane 2025). In this paper, we refer to these objects (broad Balmer line emitters or "little red dots") as low-luminosity AGNs, as they literally exhibit the defining characteristics of AGNs—active and compact. While we assume the broad lines originate from BHs, as is commonly done in other works, we note the possibility of their non-BH origins. The measurements presented in this paper, and comparisons with those of their coeval galaxy populations, are independent of the assumptions of the origins of their energy source in most cases.

To understand the nature of low-luminosity AGNs, it is crucial to constrain their large-scale environments and host dark matter halos within the context of cosmological structure formation models. Currently, our knowledge about the host galaxies of low-luminosity AGNs largely comes from SED modeling. However, this method is limited by assumptions about the intrinsic characteristics, leading to significant degeneracy (H. B. Akins et al. 2024; G. C. K. Leung et al. 2024; Y. Ma et al. 2024). It can result in a wide range of stellar masses, from extremely massive hosts ($\sim 10^{11} M_\odot$) to typical star-forming galaxies ($\sim 10^8 M_\odot$), depending on how AGN and galaxy light contributions are tuned (e.g., B. Wang et al. 2024). The clustering of low-luminosity AGNs can break this degeneracy by directly comparing their large-scale environments and dark matter halo masses with those of galaxies of similar stellar masses. Clustering analysis also provides insights to bridge the gap between low-luminosity AGNs and UV-bright quasars. UV-luminous quasars are characterized by strong large-scale clustering over a wide redshift range, consistent with host halo masses of $\sim 10^{12.5} M_\odot$ at $z > 6$ (e.g., H. Chen et al. 2022; J. Arita et al. 2023; A.-C. Eilers et al. 2024; M. Pudoka et al. 2024). If low-luminosity AGNs represent the dust-obscured phase of UV-luminous quasars (e.g., J. Lyu et al. 2024), they should inhabit similar massive dark matter halos and share comparable clustering properties. Observational studies of AGN environments and clustering properties can also inform theoretical models. For example, super-Eddington accretion has been proposed to explain some characteristics of low-luminosity AGNs, such as the V-shaped SEDs, X-ray weaknesses, and lack of variability (K. Inayoshi et al. 2024; M. Kokubo & Y. Harikane 2025; E. Lambrides et al. 2024b; A. Trinca et al. 2024). Super-Eddington accretion is predicted to occur only in low-mass hosts ($\sim 10^{10} M_\odot$) where the AGN duty cycle is low (<1%; E. Pizzati et al. 2024a). Recently, J.-T. Schindler et al. (2024) reported a low-luminosity AGN in an overdensity, with a minimum host halo mass of $10^{12.3} M_\odot$. However, systematic studies involving a larger sample of AGNs are still required. J. Matthee et al. (2024b) examined the environments within 1 cMpc of six AGNs in the A2744 lensing cluster field. Nonetheless, nonlinear physical processes may dominate on such small scales (Y. Harikane et al. 2016; T. Herard-Demanche et al. 2023). Their analysis does not extend to larger scales due to survey volume limitations. A clustering analysis on scales $\gtrsim 10$ comoving Mpc (cMpc) is crucial to probe the linear two-halo term and achieve more accurate constraints on halo masses (e.g., J. Arita et al. 2024).

In this context, the JWST/NIRCam Wide Field Slitless Spectroscopy (WFSS; T. P. Greene et al. 2016; M. J. Rieke et al. 2023) provides a unique and powerful tool for clustering analyses of low-luminosity AGNs. The JWST/NIRCam WFSS has demonstrated great efficiency in studying high-redshift emission-line galaxies. It is highly effective in identifying broad-line AGNs because of its relatively high spectral resolution, and in probing large-scale structures because of its large field of view (FOV; e.g., F. Sun et al. 2022; J. M. Helton et al. 2024; X. Lin et al. 2024). The selection function is simpler to model compared to the spectroscopic observations with pre-selection (e.g., through JWST NIRSpec). In this work, we compile AGNs and galaxies from a Complete NIRCam Grism Redshift Survey (CONGRESS) in the GOODS-N field. The dataset includes grism observations from the Cycle-1 program "First Reionization Epoch Spectroscopically Complete Observations" (FRESCO, GO-1895, PI: Oesch; P. A. Oesch et al. 2023) and the Cycle-2 program CONGRESS (GO-3577, PI Eiichi & Sun; F. Sun et al. 2025, in preparation). The two programs target the same area using the F444W and F356W grisms, respectively, together covering a total wavelength range of 3.1–5.0 μm. We collect a large number of low-luminosity AGNs at $4 \lesssim z < 6$ through their broad Hα emission lines and broadband photometric properties, and simultaneously map their surrounding environments with Hα emitters (HAEs) at the same redshift.

The paper is organized as follows. In Section 2, we introduce the datasets and methods to select galaxies and AGNs. In Section 3, we explore the large-scale environments of low-luminosity AGNs. A clustering analysis based on two-point correlation functions is presented in Section 4. Finally, in Section 5, we discuss the potential implications of our measurements for AGN evolution. Throughout this work, a flat ΛCDM cosmology is assumed, with $H_0 = 70\,\mathrm{km\,s^{-1}\,Mpc^{-1}}$, $\Omega_{\Lambda,0} = 0.7$, and $\Omega_{m,0} = 0.3$. We define $h = H_0/100 = 0.7$.

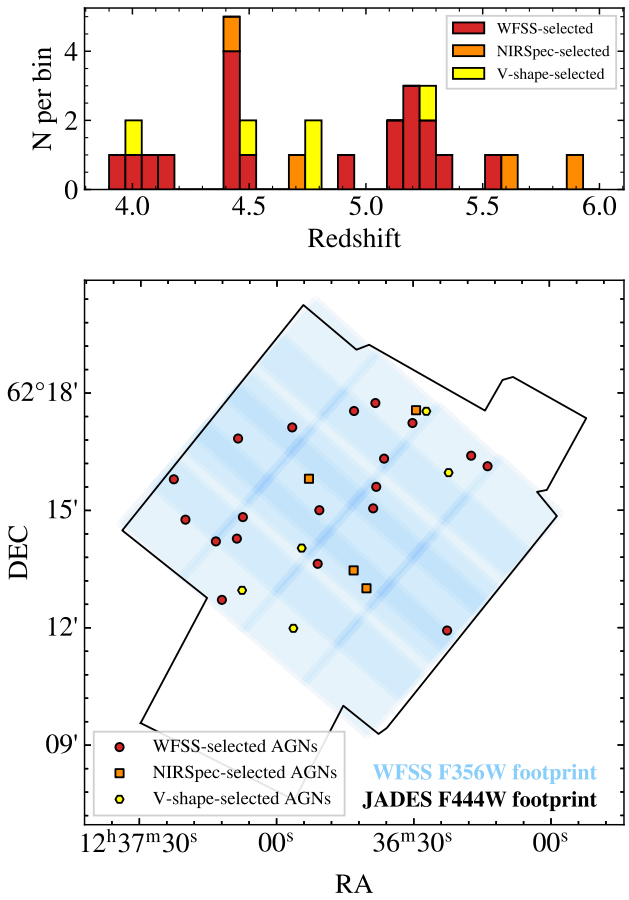

Figure 1. Top panel: the redshift distributions of AGNs in the GOODS-N field. The red, orange, and yellow histograms represent WFSS-selected, NIRSpec-selected, and V-shaped-selected samples, respectively. Bottom panel: the spatial distribution of AGNs. The blue shaded regions are the F356W WFSS (GO-3577, CONGRESS) footprint, and the black lines enclose the F444W image footprint of JADES DR3 (including FRESCO GO-1895). AGNs at $3.9 < z < 6$ are marked as red dots, orange squares, and yellow hexagons for WFSS-selected, NIRSpec-selected, and V-shaped selected sources, respectively.

2. Data and Sample

2.1. Imaging and Photometric Catalog

We use the images and photometric catalog in the GOODS-N field from the JADES Data Release 3[12] (F. D'Eugenio et al. 2024). The JADES JWST/NIRCam images in the GOODS-N field include observations from GTO programs 1181 (PI Eisenstein) and GO programs 1895 (FRESCO, PI Oesch), spanning the F090W, F115W, F150W, F182M, F200W, F210M, F277W, F335M, F356W, F410M, and F444W filters. The final mosaics cover from 56 arcmin^2 in F090W to 83 arcmin^2 in F444W (F. D'Eugenio et al. 2024). We refer to D. J. Eisenstein et al. (2023) for a detailed description of the JADES survey design, and M. J. Rieke et al. (2023) and B. Robertson et al. (2025, in preparation) for the imaging data reduction. For the direct images used for the grism spectra, the JADES images achieve a 5σ point-source depth of 29.38 mag in F444W and 29.97 mag in F356W, with aperture-corrected photometry using an $r = 0\farcs15$ circular aperture.

The JADES GOODS-N photometric catalog includes multiband photometry in the 11 JWST/NIRCam filters as mentioned above, and five HST/ACS filters (F435W, F606W, F775W, F814W, and F850LP). The HST/ACS photometry is based on images from the Hubble Legacy Fields project (G. Illingworth 2017). We refer to B. Robertson et al. (2024) for detailed source detection and photometry measurement methods. The photometric redshifts are estimated utilizing the $r = 0\farcs1$ circular aperture photometry, using `EAZY` (G. B. Brammer et al. 2008) with galaxy SED templates optimized for high-redshift sources (K. N. Hainline et al. 2024).

2.2. JWST/NIRCam Grism Spectroscopy

JWST/NIRCam WFSS observations of the GOODS-N field were obtained in both F356W and F444W filters. The Cycle-1 program, FRESCO, covers 62 arcmin^2 of the GOODS-N field through the F444W filter and row-direction grism (Grism R). The FRESCO observations in GOODS-N were split into eight pointings, and the exposure time is 8×880 s per pointing. The Cycle-2 program, CONGRESS, targets the same areas in the GOODS-N field observed by FRESCO. CONGRESS adopts the F356W filter and Grism R. CONGRESS includes 12 pointings, and the exposure time is 8×472 s per pointing. The combination of F356W and F444W grism observations results in a total wavelength coverage at 3.1–5.0 μm. The overlap area between JADES, FRESCO, and CONGRESS is about 62 arcmin^2, as illustrated in the bottom panel of Figure 1.

The grism data reduction and spectral extraction are detailed in F. Sun et al. (2025, in preparation). Here we briefly summarize the procedures. For individual exposures of grism data and their corresponding short-wavelength (SW) direct images, we performed flat-fielding, subtracted a sigma-clipped median sky background, and aligned the World Coordinate System frames. We then measured the astrometric offsets between the direct images and the JADES DR3 GOODS-N catalog. The offsets were added to the spectral tracing model for accurate wavelength calibration. The spectral tracing and wavelength calibration are based on the Commissioning, Cycle-1, and Cycle-2 calibration data taken in the SMP-LMC-58 field up to June 2024 (PID 1076, 1479, 1480, and 4449; see F. Sun et al. 2023).[13] The flux calibration is based on Cycle-1 calibration data (PID: 1076, 1536, 1537, 1538). We optimally extracted the 1D spectra based on the source morphology (K. Horne 1986).

2.3. Hα Emitters at $3.9 < z < 6$

We refer readers to X. Lin et al. (2025) for detailed descriptions of the selection procedure for line emitters. In brief, we use 51 pixel median filtering to remove the continua, extract line-only spectra, and detect emission lines in both 1D and 2D spectra. We have developed a semiautomated algorithm to identify emission-line galaxies across the redshift range $0 < z < 9$ using the photometric redshifts in the JADES catalog as priors. As a result, we selected 936 HAEs across $3.75 < z < 6.6$ with F356W and F444W Grism R in the overlapping regions of the CONGRESS and JADES imaging footprint. This work focuses on a subsample of these HAEs within the redshift range of $3.9 < z < 6$. We measured the line flux by fitting the emission line with Gaussian models convolved with the NIRCam grism line spread functions as calibrated by F. Sun et al. (2025, in preparation). The emitter

[12] https://archive.stsci.edu/hlsp/jades

[13] https://github.com/fengwusun/nircam_grism

catalog and line flux measurements will be publicly released along with F. Sun et al. (2025, in preparation).

In this work, we only consider HAEs and AGNs with Hα luminosities greater than $L_{\rm H\alpha} > 10^{41.5}$ erg s^{-1}. This is because the clustering analysis relies on luminosity function (LF) measurements, and the completeness correction for lower-luminosity bins in the Hα LFs is affected by large systematic uncertainties. For AGNs, this cut is applied to the total $L_{\rm H\alpha}$ to account for selection effects in the detectability of the Hα line. We further group galaxies with separations smaller than 10 physical kpc and 500 km s^{-1} into a system, assuming they are interacting and gravitationally bound. This separation corresponds to approximately 1.″5 at $z \approx 4$–6, consistent with the definition of a galaxy system applied to $z \sim 6$ [O III] emitters (J. Matthee et al. 2023; A.-C. Eilers et al. 2024) and well within the defining separation for mergers (e.g., D. Puskás et al. 2025). This differs from the criteria set for the LF calculation in X. Lin et al. (2025), but it follows the same method used for the HAE clustering analysis in that paper. We finally obtain 782 systems at $3.9 < z < 6$. Throughout this paper, we refer to these combined systems as galaxies for simplicity.

2.4. AGN Sample at 3.9 < z < 6

We selected AGNs from the parent HAE sample using three different sets of criteria: WFSS-based, V-shaped-based, and NIRSpec-based. All of these AGNs fall within the grism footprint. The selection criteria are outlined below.

(1) WFSS-selected broad-line AGNs. With the F356W and F444W grism covering 3.1–5.0 μm, J. Zhang et al. (2025) identified 19 broad HAEs with compact morphology[14] and FWHMs of broad Hα components exceeding 1000 km s^{-1}. In our sample, seven of these AGNs were previously reported in J. Matthee et al. (2024).

(2) NIRSpec-selected broad-line AGNs. R. Maiolino et al. (2023) identified high-redshift AGNs through prominent broad Hα emission lines in the NIRSpec R1000 grating spectra. In the GOODS-N field, they reported five objects at $4 < z < 6$ with single robust broad components. We have excluded the tentatively detected broad-line candidates and the dual broad-line candidates from their sample. Four of the five AGNs fall within the WFSS footprint but do not overlap with the WFSS-selected AGNs. These four objects show bright Hα emission lines in the grism spectra, although the broad components are overwhelmed by the background noise because of the grism's lower sensitivity and higher background level.

(3) V-shaped continuum AGNs. We have searched for compact HAEs with V-shaped SEDs among the grism-selected HAEs. V-shaped SEDs, characterized by blue UV continuum slopes ($\beta_{\rm UV}$) and red optical continuum slopes ($\beta_{\rm opt}$), have been demonstrated as effective characteristics of high-redshift AGNs (e.g., J. E. Greene et al. 2024) especially when the broad Hα fluxes are below the grism detection limit. We do not require a broad Hα line detection for V-shaped-selected AGNs.

First, we selected HAEs with a half-light radius $<0.''2$ in either the F444W or F356W filter. The robust spectroscopic redshifts ($z_{\rm spec}$) help us avoid contamination from brown dwarfs. We measured the UV continuum slope $\beta_{\rm UV}$ by fitting a power-law model to the rest-frame range 1350–3000 Å using the small-Kron-aperture KRON_S photometry (see JADES NIRCam data release; M. J. Rieke et al. 2023). The optical continuum slope $\beta_{\rm opt}$ is derived from 4000–8000 Å. We excluded bands that overlap with the Hβ + [O III], Hα lines, or the Balmer break around 3645 Å. We require at least two filters spanning over 1000 Å in the rest frame to determine $\beta_{\rm opt}$. This strict requirement ensures that the measured slopes represent the pure continuum, free from contamination by strong emission lines and flux uncertainties.

Among the 23 broad-line selected AGNs identified from WFSS and NIRSpec above, seven exhibit significant V-shaped SEDs with $\beta_{\rm UV} < 0$ and $\beta_{\rm opt} > 0$. Of the remaining 16 AGNs, seven have $\beta_{\rm opt} < 0$, while the other nine lack adequate band coverage to reliably determine $\beta_{\rm opt}$.

In addition to the broad-line AGNs above, we identify five more HAEs with robust measurements of $\beta_{\rm UV} < 0$ and $\beta_{\rm opt} > 0$.

Following the three selection criteria described above, we eventually selected a sample of 28 AGNs at $z = 3.9$–6 within the WFSS footprint for the parent HAE sample. Seven of them are also included in the photometrically selected sample in P. Rinaldi et al. (2024). The information of these 28 AGNs is summarized in Tables 1 and 2. Their spatial distribution is shown in Figure 1. All of these AGNs display Hα emission lines with $L_{\rm H\alpha} > 10^{41.5}$ erg s^{-1} in the grism spectra, satisfying the selection criteria for HAEs in the clustering analysis.

3. Diverse Environments of JWST-selected High-redshift AGNs

In this section, we study the large-scale environments of AGNs at $z = 3.9$–6 based on the grism-selected HAEs.

3.1. Overdensity Field δ of High-redshift AGNs

We calculate the overdensity field, δ, for each AGN based on the number density of HAEs within a volume of $(15\,h^{-1}\,{\rm cMpc})^3$, which equals the volumes defined in Y.-K. Chiang et al. (2013) and has been widely adopted in the literature (e.g., Y.-K. Chiang et al. 2014; O. Cucciati et al. 2014; Z. Cai et al. 2016; J. M. Helton et al. 2024; S. Lim et al. 2024). We center a cylinder with a radius of $8.5\,h^{-1}$ cMpc and a length of $15\,h^{-1}$ cMpc on the AGN, and calculate the galaxy density, n, within its volume by counting all enclosed galaxies. The WFSS footprint edge is taken into account. To calculate the mean galaxy density, $\bar{n}$, we use the random galaxy catalog from the HAE autocorrelation analysis in X. Lin et al. (2025). The random galaxy catalog is designed to simulate a uniform distribution of galaxies without any clustering signal, while following the same selection function as the observed sample. The line fluxes of random galaxies are drawn from the Hα luminosity functions, and the completeness model is applied to account for selection effects. We count the random galaxies within the same volume and then scale the value to match the total HAE number density within the FOV. The overdensity field is computed as $\delta = n/\bar{n} - 1$. The uncertainty of δ includes Poisson fluctuations of the observed galaxies and dispersion in

[14] The criteria for compactness is defined based on circular aperture photometry $\frac{\text{F444W flux within r = 0.2″}}{\text{F444W flux within r = 0.1″}} \leqslant 1.2$, as justified in J. Zhang et al. (2025).

Table 1
Broad-line Selected AGN Sample in This Work

ID	R.A.	Decl.	z_{spec}	Selection	$\log L_{H\alpha,broad}$ (erg s^{-1})	$FWHM_{H\alpha,broad}$ (km s^{-1})	$\log M_{BH}$ ($M_\odot$)	β_{UV}	β_{opt}
1087315	189.3336	62.2462	3.91	WFSS	42.09 ± 0.05	1514 ± 183	7.01 ± 0.11	-0.44 ± 1.02	-1.47 ± 0.13
1082263	189.2126	62.2274	3.98	WFSS	41.96 ± 0.07	1083 ± 205	6.65 ± 0.17	-1.70 ± 0.09	-0.20 ± 0.09
1089568	189.1518	62.2722	4.05	WFSS	42.22 ± 0.04	1461 ± 143	7.04 ± 0.09	-1.16 ± 0.43	-1.20 ± 0.10
1029154	189.1590	62.2602	4.17	WFSS	42.33 ± 0.04	2003 ± 225	7.38 ± 0.10	-1.56 ± 0.19	0.74 ± 0.17
1008411	189.2111	62.2503	4.41	WFSS	42.11 ± 0.11	3281 ± 757	7.72 ± 0.21	-0.74 ± 0.32	0.72 ± 0.12
1008671	189.1618	62.2511	4.41	WFSS	42.54 ± 0.02	2272 ± 95	7.59 ± 0.04	-1.53 ± 0.13	0.13 ± 0.11
1086855	189.2865	62.2381	4.41	WFSS	42.40 ± 0.06	1724 ± 271	7.28 ± 0.14	-1.01 ± 0.19	0.58 ± 0.12
1086784	189.3057	62.2369	4.41	WFSS	42.15 ± 0.07	3179 ± 504	7.71 ± 0.14	-0.13 ± 1.26	-0.10 ± 0.15
1033320	189.1258	62.2874	4.48	WFSS	42.04 ± 0.08	1951 ± 398	7.22 ± 0.19	-1.65 ± 0.12	-0.67 ± 0.26
1085355	189.0944	62.1990	4.88	WFSS	42.35 ± 0.03	1800 ± 158	7.29 ± 0.08	-1.76 ± 0.70	⋯
1090253	189.2855	62.2808	5.09	WFSS	42.41 ± 0.03	1455 ± 105	7.13 ± 0.07	-1.05 ± 0.75	⋯
1014406	189.0721	62.2734	5.15	WFSS	42.34 ± 0.07	3212 ± 639	7.81 ± 0.18	-1.61 ± 0.16	⋯
1034620	189.1598	62.2959	5.19	WFSS	42.68 ± 0.02	1077 ± 71	6.99 ± 0.06	-1.43 ± 0.06	⋯
1090549	189.2359	62.2855	5.19	WFSS	42.21 ± 0.07	1721 ± 307	7.19 ± 0.16	-1.88 ± 0.24	⋯
9994014	189.3001	62.2120	5.23	WFSS	42.61 ± 0.03	2084 ± 156	7.55 ± 0.07	$-2.04^{+0.70}_{-0.93}$	$2.00^{+1.12}_{-0.82}$
1088832	189.3443	62.2634	5.24	WFSS	43.10 ± 0.02	2255 ± 91	7.85 ± 0.04	-1.27 ± 0.20	⋯
1013188	189.0571	62.2689	5.25	WFSS	42.33 ± 0.03	1957 ± 147	7.36 ± 0.07	-1.44 ± 0.29	⋯
1020514	189.1793	62.2925	5.36	WFSS	42.40 ± 0.03	1612 ± 140	7.22 ± 0.08	-1.91 ± 0.07	-0.32 ± 0.37
1087388	189.2810	62.2473	5.54	WFSS	43.52 ± 0.01	2964 ± 55	8.29 ± 0.02	-0.30 ± 0.19	⋯
1011836	189.2206	62.2637	4.41	NIRSpec	$41.86^{+0.03}_{-0.03}$	1451^{+98}_{-105}	7.13 ± 0.31	-0.94 ± 0.11	-2.14 ± 0.08
1020621	189.1225	62.2929	4.68	NIRSpec	$42.00^{+0.03}_{-0.03}$	1638^{+148}_{-150}	7.30 ± 0.31	-1.18 ± 0.17	0.88 ± 0.33
1001093	189.1797	62.2246	5.60	NIRSpec	$41.86^{+0.04}_{-0.03}$	1662^{+203}_{-165}	$7.36^{+0.32}_{-0.31}$	-1.30 ± 0.30	0.12 ± 0.23
1061888	189.1680	62.2170	5.87	NIRSpec	$42.15^{+0.03}_{-0.02}$	1375^{+97}_{-127}	7.22 ± 0.31	-1.96 ± 0.17	⋯

Note. ID refers to the source ID in the JADES DR3 photometric catalog (F. D'Eugenio et al. 2024), and z_{spec} is the spectroscopic redshift measured from the NIRCam WFSS data. (ID 9994014 is not included in the JADES DR3 catalog because of a diffraction-spike mask, but is reported in J. Matthee et al. 2024.) SELECTION indicates the different selection criteria outlined in Section 2.4. The broad Hα luminosities ($L_{H\alpha,broad}$), FWHMs of the broad Hα emission lines ($FWHM_{H\alpha,broad}$), and black hole masses (M_{BH}) for the WFSS-selected AGNs are taken from J. Zhang et al. (2025), while those for the NIRSpec-selected AGNs are from R. Maiolino et al. (2023). The UV (β_{UV}) and optical (β_{opt}) slopes are calculated using KRON_S photometry (Kron radius = 1.2) with at least two strong line-free bands spanning >1000 Å in the rest frame.

Table 2
The V-shaped SED-selected AGNs in This Work, as a Complement to the Broad-line Sample in Table 1

ID	R.A.	Decl.	z_{spec}	Selection	β_{UV}	β_{opt}
1055902	189.2348	62.2000	4.02	V-shaped SED	-1.82 ± 0.19	0.05 ± 0.30
1029892	189.0928	62.2662	4.47	V-shaped SED	-0.85 ± 0.23	0.14 ± 0.29
1066100	189.2272	62.2341	4.76	V-shaped SED	-1.60 ± 0.27	0.79 ± 0.31
1081040	189.2816	62.2161	4.76	V-shaped SED	-1.71 ± 0.20	1.30 ± 0.25
1020485	189.1131	62.2924	5.27	V-shaped SED	-1.70 ± 0.23	0.60 ± 0.27

Note. ID refers to the source ID in the JADES DR3 photometric catalog, and z_{spec} is the spectroscopic redshift measured from the NIRCam WFSS data.

the random galaxy distribution across different random galaxy realizations.

The overdensity δ around AGNs is shown in Figure 2. The JWST AGNs are located in highly diverse large-scale environments. Their δ values range from -0.56, indicating underdense environments, to 10.56, representing an extreme overdensity. Among them, 10 AGNs (36% ± 9% assuming a binomial distribution) are in overdense regions with $\delta > 3$, while the remaining 18 AGNs (64% ± 9%) are in average or underdense regions. We identify two extreme protoclusters at $z = 4.41$ and $z = 5.19$. The protocluster at $z \approx 4.41$ contains five AGNs and 92 HAEs after applying the luminosity cut and grouping. These AGNs show overdensities ranging from $\delta = 6.85$ to 10.51. Six AGNs at $5.16 < z < 5.29$ are found in the filamentary structure at $z = 5.19$ (T. Herard-Demanche et al. 2023; F. Sun et al. 2024). The structure consists of three galaxy groups, with 93 galaxies at $z = 5.19$, 22 galaxies at $z = 5.22$, and 19 galaxies at $z = 5.27$. Among the six AGNs, two are associated with the $z = 5.19$ galaxy group, and two are associated with the $z = 5.22$ and $z = 5.27$ galaxy groups. These four exhibit $\delta = 5.17$–10.56. The remaining two AGNs reside between these groups, with $\delta = 3.02$ and 1.38, respectively. We show the 3D structures of both protoclusters in Figure 3.

As a baseline for comparison, we also calculate the δ values for HAEs at similar redshifts. Among the 782 HAEs at $3.9 < z < 6$, 232 (30% ± 2%) lie in regions with $\delta > 3$. The fraction of galaxies in overdense regions is broadly consistent with that of the AGNs within 1σ. We conclude that, statistically, AGNs in our sample are not preferentially located in denser large-scale environments compared to star-forming galaxies.

3.2. Dependence of AGN Properties on Their Environments

We explore the correlation between δ and the broad-line Hα luminosity ($L_{H\alpha,broad}$), the FWHMs of the broad Hα

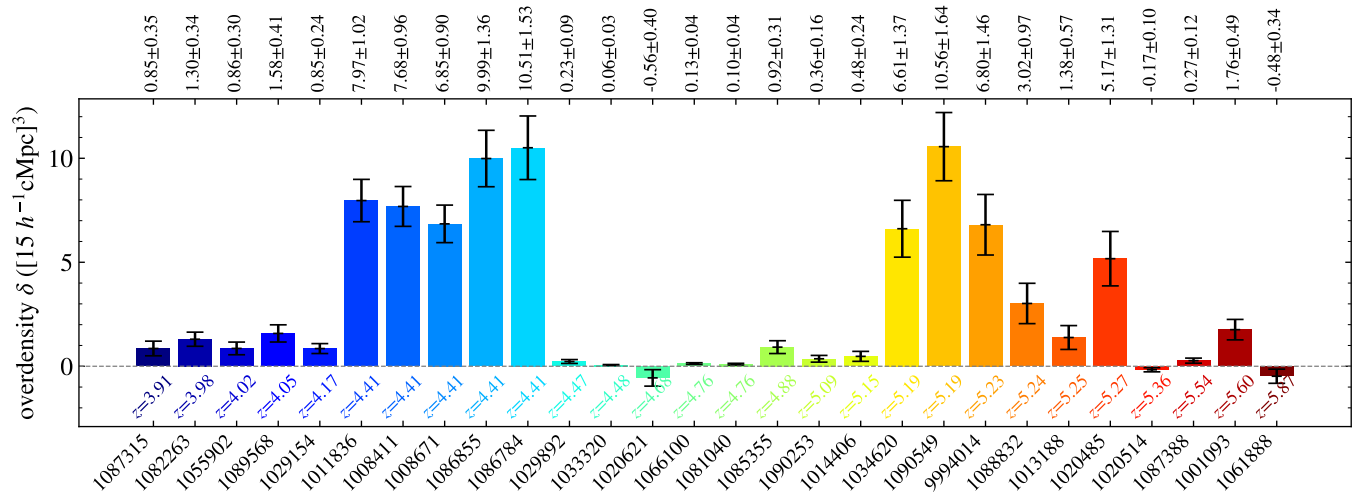

Figure 2. The overdensity fields δ over a volume of $(15\,h^{-1}\,\mathrm{cMpc})^3$ for AGNs at $3.9 < z < 6$. The AGNs are ordered and color-coded by their redshift, with their IDs shown on the x-axis. The δ value is labeled at the top of each AGN.

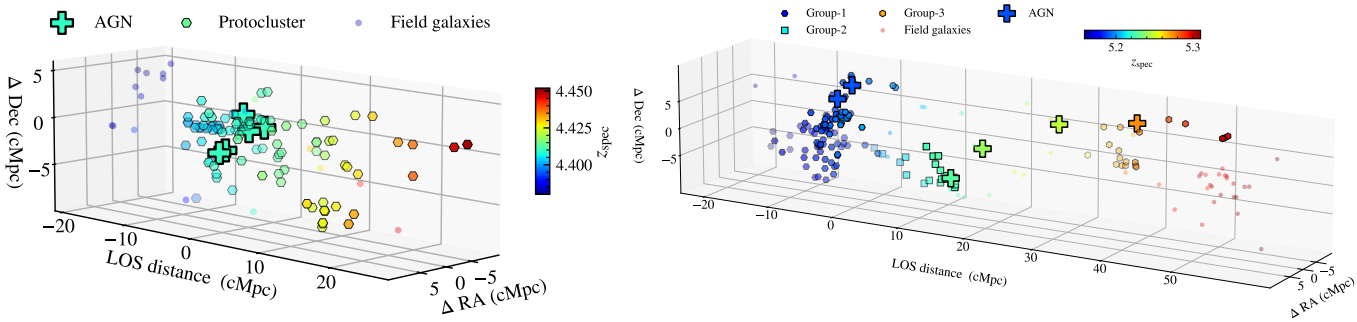

Figure 3. The 3D large-scale structure of the protocluster at $z \approx 4.41$ (left) and $z \approx 5.19$ (right), after the luminosity cut of $10^{41.5}$ erg s^{-1} and grouping within 500 pkpc and 500 km s^{-1}. They host five and six AGNs, respectively. The coordinates of the $z \approx 4.41$ structure are with respect to (R.A., decl., z) = (189.21355, 62.24861, 4.41), and the coordinates of the $z \approx 5.19$ structure are with respect to (R.A., decl., z) = (189.20403, 62.23787, 5.195). All sources are color-coded by their redshifts, with the plus indicating AGNs, hexagons/squares indicating the protocluster members, and dots indicating field galaxies.

(FWHM$_{\mathrm{H}\alpha,\mathrm{broad}}$), and the BH mass ($M_{\mathrm{BH}}$). We use only the broad-line selected AGNs from the grism and NIRSpec (R. Maiolino et al. 2023; J. Zhang et al. 2025), for which these parameters can be measured. We note that precise M_{BH} values are uncertain due to the unclear nature of these low-luminosity AGNs. We follow the common practice of deriving BH masses from $L_{\mathrm{H}\alpha,\mathrm{broad}}$ and FWHM$_{\mathrm{H}\alpha,\mathrm{broad}}$ to examine the potential correlation. In this work, M_{BH} is calculated following A. E. Reines & M. Volonteri (2015), as a result of $L_{\mathrm{H}\alpha,\mathrm{broad}}$ and FWHM$_{\mathrm{H}\alpha,\mathrm{broad}}$ ($M_{\mathrm{BH}} \propto \mathrm{FHWM}^{2.06}_{\mathrm{H}\alpha,\mathrm{broad}} L^{0.47}_{\mathrm{H}\alpha,\mathrm{broad}}$). We perturb these parameters within their uncertainties to estimate the uncertainties in the correlation coefficient.[15] The correlations between $L_{\mathrm{H}\alpha,\mathrm{broad}}$, FWHM$_{\mathrm{H}\alpha,\mathrm{broad}}$, and M_{BH} with δ are shown in Figure 4. No clear correlation is found for $L_{\mathrm{H}\alpha,\mathrm{broad}}$, FWHM$_{\mathrm{H}\alpha,\mathrm{broad}}$, or M_{BH}, as the Kendall's τ analysis yields $p > 0.05$.[16]

We define the AGN fraction in this work as the proportion of AGNs that meet any of the three selection criteria (Section 2.4) among all grism-selected HAEs. The averages are 3.7% at $3.9 < z < 5$, 4.0% at $5 < z < 6$, and 3.9% for the combined range $3.9 < z < 6$. We calculate the overdensity, δ, for all HAEs in the range $3.9 < z < 6$ using the same method described in Section 3.1, and estimate the AGN fraction within each fixed δ range. Figure 5 shows the AGN fraction as a function of δ. The uncertainties are calculated assuming a binomial distribution for the AGN fraction. The Kendall's τ analysis implies no significant dependence of AGN fraction on δ, with a correlation coefficient τ consistent with 0 and a p-value much greater than 0.05. We note that the AGN fractions shown here do not include corrections for selection functions or completeness, particularly for those selected through NIRSpec. For comparison, in Figure 5 we also show AGN fractions compiled from NIRSpec broad-line selections (Y. Harikane et al. 2023; R. Maiolino et al. 2023; I. Juodžbalis et al. 2025) and from grism-based broad-line selections (X. Lin et al. 2024; J. Matthee et al. 2024). Although the AGN fractions are luminosity-dependent and may be affected by cosmic variance, the absence of correlations in our results is less susceptible to these factors. A more accurate determination of the AGN fraction will require future observations with higher sensitivity, more uniform selection criteria, and careful accounting for selection effects.

The overdensity, δ, on $15\,h^{-1}$ cMpc scales is primarily driven by the large-scale structure dominated by the linear two-halo terms (e.g., Y. Harikane et al. 2016; Y. Herrero Alonso et al. 2023). The lack of dependence of δ on M_{BH}

[15] We use `pymccorrelation` (https://github.com/privong/pymccorrelation) to implement the perturbation (P. A. Curran 2014; G. C. Privon et al. 2020).

[16] The p-value denotes the probability of obtaining the current result if the correlation coefficient were zero (no correlation). If p is lower than 0.05, the correlation coefficient is statistically significant.

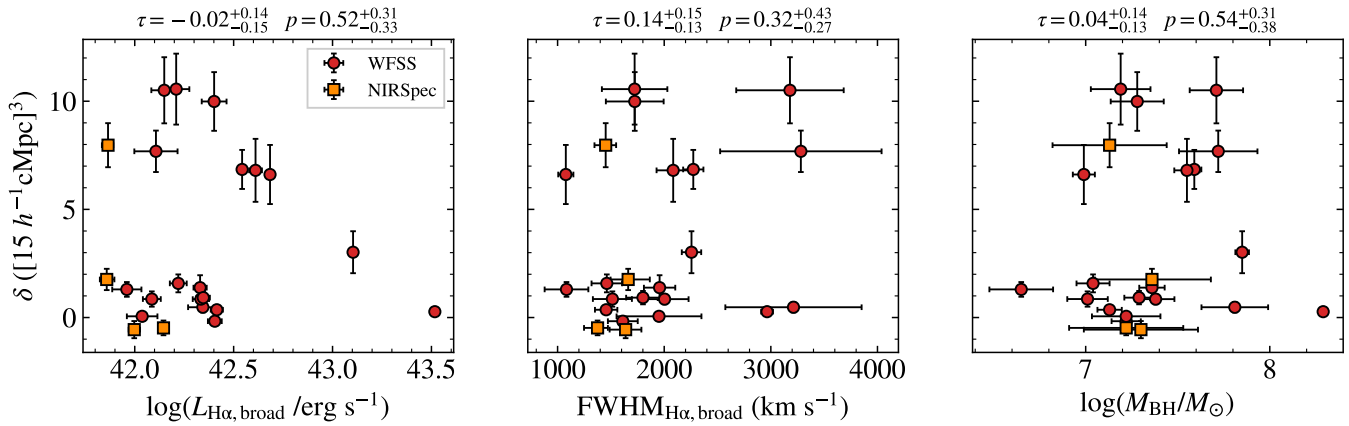

Figure 4. The overdensity fields δ of AGNs vs. their broad Hα luminosities (left panel), FWHMs of their broad Hα lines (middle panel), and BH masses (right panel). The red dots represent the WFSS-selected broad-line AGNs, and the orange squares are the NIRSpec-selected broad-line AGNs. The Kendall's τ analysis, with τ and p labeled on top of each panel, suggests no significant correlation between δ and the three parameters.

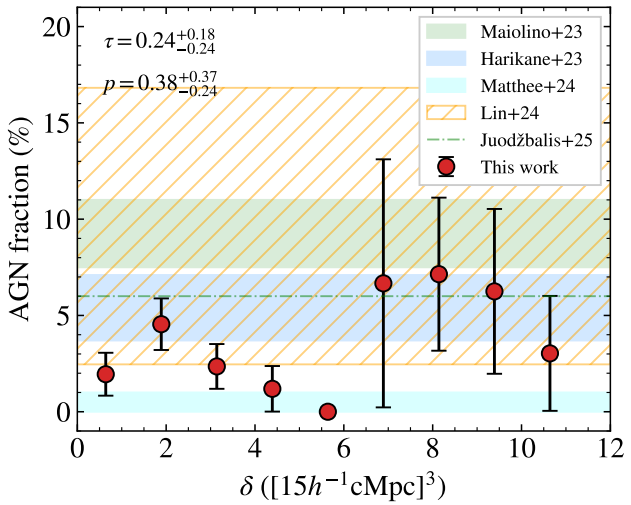

Figure 5. AGN fraction among the star-forming galaxies vs. the overdensity field δ. The Kendall's τ statistic and the associated probability p are labeled at the top left, revealing no significant correlation between AGN fraction and δ. The AGN fractions from literature studies are shown as green, blue, cyan, and orange shaded regions and green dashed–dotted lines for reference (Y. Harikane et al. 2023; R. Maiolino et al. 2023; X. Lin et al. 2024; J. Matthee et al. 2024; I. Juodžbalis et al. 2025). Note that these different AGN fractions are luminosity-dependent and subject to cosmic variance and selection effects.

implies significant scatter in the relation between large-scale environments and black hole (BH) mass in high-redshift AGNs. On the other hand, the bolometric luminosity and Eddington ratios can be derived using $L_{\rm H\alpha,broad}$ and FWHM$_{\rm H\alpha,broad}$ by applying the empirical relations for typical type-1 AGNs to these low-luminosity AGNs (J. E. Greene & L. C. Ho 2005; B. Trakhtenbrot et al. 2011), although this may not be accurate but is commonly adopted (e.g., R. Maiolino et al. 2023; X. Lin et al. 2024; J. Matthee et al. 2024). In this context, the lack of correlation of δ with respect to $L_{\rm H\alpha,broad}$ and FWHM$_{\rm H\alpha,broad}$ suggests that bolometric luminosity and Eddington ratios do not correlate with δ either. These results suggest that the large-scale environment on scales >10 cMpc does not significantly affect BH growth and AGN evolution on smaller, parsec scales.

In contrast, J. Matthee et al. (2024b) found that overdensity within 1 cMpc is positively correlated with $M_{\rm BH}$, particularly when including measurements from 10 high-redshift AGNs and five quasars (A.-C. Eilers et al. 2024). X. Lin et al. (2024) also reported tentative evidence of small-scale clustering around one low-luminosity AGNs, with three neighboring galaxies located within 30 kpc. Our WFSS observations are not as deep as those in J. Matthee et al. (2024b), which were conducted in a lensing cluster field with longer exposures, limiting our ability to probe overdensities within 1 cMpc. The 1 cMpc scale is around the typical transition point between the dominance by nonlinear one-halo terms and linear two-halo terms for high-redshift galaxies (e.g., Y. Harikane et al. 2016; Y. Herrero Alonso et al. 2023). The differing environmental effects on $M_{\rm BH}$ at scales <1 cMpc and >10 cMpc suggest that BH growth may be more strongly influenced by local nonlinear processes such as mergers. Alternatively, processes occurring on cosmological scales, such as the gas accretion from the large-scale cosmic web, have a weaker impact. These large-scale activities may require a longer time to come into effect and impact the small-scale BH activities. Future deep spectroscopic surveys are required to provide further insights by probing multiscale environments of a large AGN sample across a wide range of $M_{\rm BH}$.

4. The Clustering Analysis of High-redshift AGNs

As illustrated in Section 3, there is significant variance in the environments of high-redshift AGNs. We therefore investigate their average population-level clustering properties in the context of large-scale structure of star-forming galaxies at the same cosmic epochs. For this clustering analysis, we focus exclusively on the 26 AGNs that meet the grism broad-line selection and V-shaped SED criteria. Two of the four NIRSpec-selected AGNs meet the V-shaped SED criteria and are therefore included in the clustering analysis. We do not include the remaining two NIRSpec-selected AGNs because of the limitation in quantifying their selection function via the Micro Shutter Array (MSA) design. The MSA targets must be pre-selected, resulting in a biased search.

4.1. The Projected Surface Density Excess

We first compare the galaxy surface number density distributions centered on AGNs and HAEs. We define the

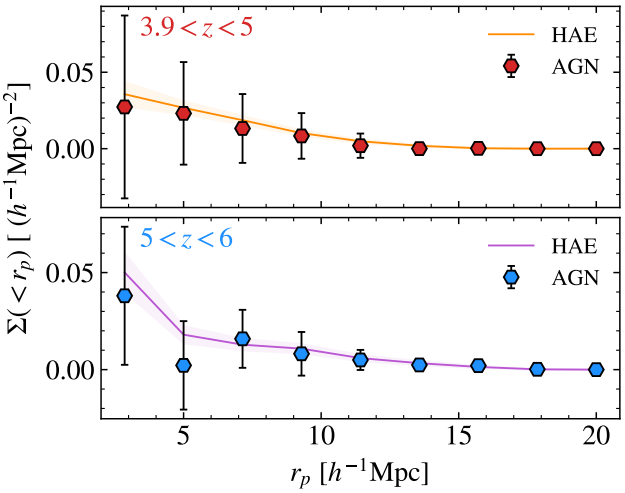

Figure 6. The projected surface density excess of AGNs compared to that of HAEs. The lines represent the median of $\Sigma(<r_p)$ for HAEs, with the shaded regions indicating the 1σ range. The hexagons denote the median of $\Sigma(<r_p)$ for AGNs. The error bars indicate the 1σ level of the $\Sigma(<r_p)$ values.

projected surface density excess within a radius of r_p by

$$\Sigma(<r_p) = \frac{N(<r_p)}{A(<r_p)} - \frac{N_{\rm all}}{A_{\rm all}}, \quad (1)$$

where r_p is the projected distance on the sky plane. $N(<r_p)$ is the number of HAEs within a cylindrical volume of radius r_p and line-of-sight length $8\,h^{-1}$ Mpc. The line-of-sight length corresponds to approximately 1000 km s^{-1} at $z \approx 5$. We have tested and confirmed that this length effectively captures the large-scale structure signal along the line of sight while preserving optimal signal-to-noise ratios for the clustering measurements. $A(<r_p)$ is the area on the projected sky plane within radius r_p. $N_{\rm all}$ and $A_{\rm all}$ are the total galaxy number and projected area of the WFSS footprint, respectively. The value $N_{\rm all}/A_{\rm all}$ is used to evaluate the average projected surface density across the entire survey area. $\Sigma(<r_p)$ represents the excess in the galaxy number surface density within a radius of r_p, relative to the average surface density.

We calculate $\Sigma(<r_p)$ for each AGN and HAE. The median projected surface density excess of AGNs and HAEs at $3.9 < z < 5$ and $5 < z < 6$ is presented in Figure 6. The projected surface density excess of AGNs is consistent with that of HAEs, although it shows a large variance at $r_p < 10\,h^{-1}$ Mpc. The variances arise from the diversity of AGN environments, as well as the limited survey volume and depth, which primarily dominate the uncertainty in the two bins at $r_p < 5\,h^{-1}$ Mpc. Nevertheless, the broad agreement in the projected surface density excess of AGNs and HAEs suggests that star-forming galaxies do not have stronger clustering around AGNs, compared to the normal galaxy–galaxy clustering.

4.2. The Cross-correlation between Hα Emitters and AGNs

Because the sample size of AGNs is too small for autocorrelation analysis, we instead study the cross-correlation between HAEs and AGNs to examine the clustering of AGNs. We adopt the LS estimators (S. D. Landy & A. S. Szalay 1993) as follows:

$$\xi_{ag}(\boldsymbol{r}) = \frac{N_{\rm r}(N_{\rm r}-1)}{2N_{\rm a}N_{\rm g}}\frac{AG(\boldsymbol{r})}{RR(\boldsymbol{r})} - \frac{N_{\rm r}-1}{2N_{\rm g}}\frac{GR(\boldsymbol{r})}{RR(\boldsymbol{r})} - \frac{N_{\rm r}-1}{2N_{\rm a}}\frac{AR(\boldsymbol{r})}{RR(\boldsymbol{r})} + 1, \quad (2)$$

where N_a is the number of AGNs, AG represents the number of AGN-HAE pairs and AR represents the number of AGN-random pairs. We compute the volume-averaged projected χ_V following J. F. Hennawi et al. (2006):

$$\chi_V(r_p) = \frac{2}{V}\int_{r_{p,\rm min}}^{r_{p,\rm max}}\int_0^{r_{\pi,\rm max}} \xi(r_p, r_\pi) 2\pi r_p\, dr_p\, dr_\pi, \quad (3)$$

where $r_{\pi,\rm max}$ is the integration limit along the line-of-sight direction. We set $r_{\pi,\rm max}$ to be $8\,h^{-1}$ cMpc, corresponding to approximately 1000 km s^{-1} at $z \approx 4$–6 and can effectively capture the clustering signals of large-scale structure. V is the volume of the cylindrical shell in the r_p bin ($r_{p,\rm min} < r_p < r_{p,\rm max}$), which can be expressed as $V = \pi(r_{p,\rm max}^2 - r_{p,\rm min}^2)\cdot r_{\pi,\rm max}$. We construct the covariance matrix using bootstrapping. Each time, we sample the AGN and HAE catalogs with replacement and calculate the cross-correlation using different random catalog realizations. The uncertainties are derived from the diagonal of the covariance matrix.

The measured cross-correlations for all AGNs and HAEs at $3.9 < z < 5$ and $5 < z < 6$, including those in protoclusters, are shown in Figure 7. We also calculate χ_V for field AGNs and HAEs by excluding the two protoclusters at $z = 4.41$ and 5.19 shown in Figure 3. We parameterize the correlation functions by a power law:

$$\xi(r) = (r/r_0)^{-\gamma}, \quad (4)$$

where r_0 denotes the characteristic scale length (i.e., $\xi(r_0) = 1$). The best-fit power-law models are listed in Table 3. For comparison, we also list the best-fit parameters for the field HAE autocorrelation functions and those of all HAEs including protocluster member galaxies. The HAE clustering analysis is described in X. Lin et al. (2025). While the power-law slope γ for field AGN-HAE cross-correlations is consistent with the typical range of 1.6–2.0 reported in the literature (e.g., J. F. Hennawi et al. 2006; J. E. Geach et al. 2012; A.-C. Eilers et al. 2024), the slopes of AGN-HAE cross-correlations including protocluster members are flatter ($\gamma = 1.27$, 1.06 at $z \approx 3.9$–5 and $z \approx 5$–6, respectively). These flat γ values are also observed in the HAE autocorrelations with protocluster galaxies. The flattening is attributed to the filamentary geometry of protoclusters, which is clearly reflected in the 2D $\xi(r_p, r_\pi)$ planes. We refer interested readers to X. Lin et al. (2025) for a more detailed discussion of the geometry effect. To better compare the amplitudes of AGN-HAE cross-correlations with those of HAE autocorrelations, we fix the γ of the AGN-HAE cross-correlations to match that of the HAE autocorrelations.

The AGN-HAE cross-correlation at $3.9 < z < 5$, when including sources from the $z \approx 4.41$ protocluster, exhibits a higher amplitude than the HAE autocorrelation. This is due to the higher fraction of AGNs (five out of 16, or 31%) residing in the protocluster compared to HAEs (92 out of 482, or 19%). Despite this, the two amplitudes remain consistent within 2σ.

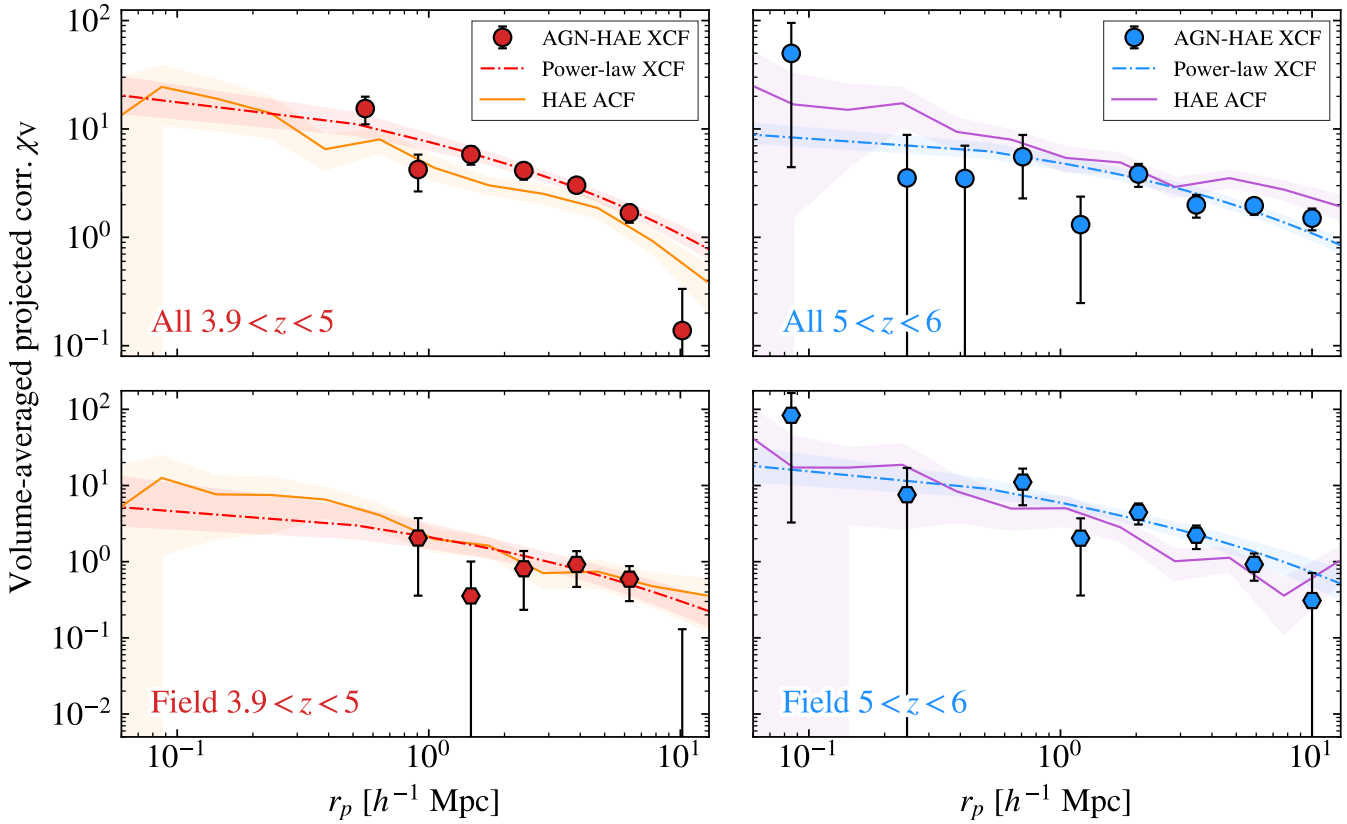

Figure 7. The volume-averaged AGN-HAE cross-correlation compared to the HAE autocorrelation. Top panels: the correlation functions consider all HAEs and AGNs, including those in the protoclusters. In the top-left panel, the red dots show the cross-correlation between AGNs and HAEs at $3.9 < z < 5$. The dashed–dotted red line and red shaded region denote the best-fit power-law model and its uncertainty. The orange line and orange shaded regions are the HAE autocorrelation and its uncertainty at $4 \lesssim z < 5$. In the top-right panel, the blue dots show the cross-correlation between AGNs and HAEs at $5 < z < 6$, with the dashed–dotted blue line indicative of the best-fit power-law model. The purple line and purple shaded regions are the HAE autocorrelation and its uncertainty at $5 < z < 6$. Bottom panels: similar to the top panels, but for AGNs and HAEs in the field. We exclude the $z \approx 4.41$ and $z \approx 5.19$ protoclusters from both the AGN-HAE cross-correlation and HAE autocorrelation.

Table 3
Best-fit Power-law Parameters for the AGN-HAE Cross-correlations Presented for Two Cases: Including AGNs and Galaxies within the Protoclusters (ALL) and Including only the Field AGNs and Galaxies (FIELD)

		ALL		FIELD	
Parameter	Unit	$3.9 < z < 5$	$5 < z < 6$	$3.9 < z < 5$	$5 < z < 6$
γ	⋯	$1.27^{+0.16}_{-0.15}$	$1.08^{+0.10}_{-0.06}$	$1.35^{+0.42}_{-0.25}$	$1.30^{+0.27}_{-0.20}$
r_0	(h^{-1} Mpc)	$12.37^{+2.30}_{-1.70}$	$11.83^{+1.58}_{-1.37}$	$4.26^{+0.83}_{-0.70}$	$9.94^{+3.06}_{-2.25}$
γ (fixed)	⋯	1.34	1.02	1.59	1.63
r_0 (γ fixed)	(h^{-1} Mpc)	$11.75^{+0.94}_{-0.87}$	$12.63^{+1.45}_{-1.35}$	$4.26^{+0.70}_{-0.61}$	$7.66^{+0.90}_{-0.81}$
r_0^{gg}	(h^{-1} Mpc)	$8.29^{+1.66}_{-1.21}$	$19.71^{+3.38}_{-2.90}$	$4.61^{+1.00}_{-0.68}$	$6.23^{+1.68}_{-1.13}$
γ^{gg}	⋯	$1.34^{+0.13}_{-0.14}$	$1.02^{+0.03}_{-0.02}$	$1.59^{+0.23}_{-0.25}$	$1.63^{+0.24}_{-0.26}$
$\log M_h$	($M_\odot$)	$11.21^{+0.36}_{-0.33}$	$11.06^{+0.36}_{-0.32}$	$11.21^{+0.35}_{-0.32}$	$11.04^{+0.34}_{-0.32}$
$\log M_*$	($M_\odot$)	$8.57^{+0.80}_{-0.71}$	$8.41^{+0.79}_{-0.70}$	$8.55^{+0.77}_{-0.73}$	$8.36^{+0.74}_{-0.70}$
b_g	⋯	⋯	⋯	4.11 ± 0.12	5.90 ± 0.08
b_a	⋯	⋯	⋯	2.95 ± 0.99	8.19 ± 1.81
$\log M_{h,b_g}$	($M_\odot$)	⋯	⋯	11.20 ± 0.05	11.25 ± 0.02
$\log M_{h,b_a}$	($M_\odot$)	⋯	⋯	$10.57^{+0.56}_{-0.97}$	$11.76^{+0.26}_{-0.38}$

Note. The parameters r_0 and γ represent the characteristic scale length and the slope of the AGN-HAE cross-correlation, respectively. For comparison, we also provide the scale length (r_0^{gg}) and slope (γ^{gg}) of the HAE autocorrelations, along with the derived halo masses (M_h) and stellar masses ($M_\star$) from UniverseMachine (P. Behroozi et al. 2019). The values represent the median of the M_h and $M_\star$ distributions. The 1σ ranges are based on the 16th and 84th percentiles of these distributions. As a complement, we also present the measured bias for field HAEs (b_g) and AGNs (b_a), and the corresponding halo masses derived from the biases (M_{h,b_g}, M_{h,b_a}).

At $5 < z < 6$, the AGN-HAE cross-correlation, when including the $z = 5.19$ protocluster, has a lower amplitude than the HAE autocorrelation. Overall, variations in the AGN-HAE cross-correlation that include all HAEs are primarily driven by cosmic variance introduced by the two protoclusters. In contrast, at $3.9 < z < 5$ and $5 < z < 6$ (bottom

panel of Figure 7), the field AGN-HAE cross-correlation amplitudes are consistent with those of the field HAE autocorrelation. When both correlation functions are fitted with the same power-law slope (γ), their amplitudes agree within 1σ (Table 3). We conclude that the AGN-HAE cross-correlation has an amplitude comparable to that of the HAE autocorrelation. This consistency in the correlation function aligns with the similar amplitude of the projected surface density excess for AGNs and HAEs, as discussed in Section 4.1.

Based on the linear perturbation theory (see an overview about galaxy bias in V. Desjacques et al. 2018), the two-point correlation functions for HAEs, $\xi_{gg}(\boldsymbol{r})$, and for AGNs and HAEs, $\xi_{ag}(\boldsymbol{r})$, can be expressed as

$$\xi_{ag}(\boldsymbol{r})^2 = \xi_{aa}(\boldsymbol{r})\xi_{gg}(\boldsymbol{r}) \quad (5)$$

$$= b_a b_g \xi^2_{mm}(\boldsymbol{r}), \quad (6)$$

where b_g and b_a are the bias factors for the enhancement of the perturbation in HAE and AGN number densities, and $\xi_{mm}(\boldsymbol{r})$ is the dark matter autocorrelation function. According to Equation (5), the comparable amplitudes of ξ_{ag} and ξ_{gg} suggest comparable amplitudes of ξ_{aa} and ξ_{gg}, and thus, b_g and b_a should be similar. According to the linear bias theory, we conclude that AGNs and HAEs in our sample reside in dark matter halos of similar mass.

5. Discussion

5.1. Implications for the AGN Host Dark Matter Halo Masses

The similar amplitudes of the HAE autocorrelation function, ξ_{gg}, and the AGN-HAE cross-correlation function, ξ_{ag}, suggest that high-redshift AGNs in our sample reside in dark matter halos with masses comparable to those of star-forming galaxies at the same redshifts. In X. Lin et al. (2025), we derive the dark matter halo masses (M_h) of HAEs by comparing the HAE autocorrelation with UniverseMachine simulations (P. Behroozi et al. 2019). The comparison accounts for both sample and cosmic variance, including the impact of large-scale structure geometry on the power-law shape of clustering. We adopt the M_h values of HAEs for AGNs, as shown in Table 3. The M_h values are taken as the medians of the simulated halo mass distributions, with the 16th and 84th percentiles indicating the scatter. Note that we adopt M_h defined for (sub)halos. Each (sub)halo hosts an individual galaxy, whether central or satellite, which cannot be distinguished based on our observations. The derived halo mass M_h is approximately $10^{11} M_\odot$ for both protocluster members and field galaxies.

As a complement, we estimate the bias for both HAEs and AGNs. Since the correlation functions of HAEs and AGNs in the full sample are affected by the protocluster geometry, we restrict the measurements to the field sample. The biases are derived by fitting the measured correlation functions at $r_p > 1\,h^{-1}$ Mpc to that of the underlying dark matter field, assuming the transfer function model from CAMB (A. Lewis & A. Challinor 2011) and bias model of J. L. Tinker et al. (2010). We first obtain the bias for HAEs (b_g) from the HAE autocorrelation function, fix it, and then fit the bias for AGNs (b_a) following Equation (6). The results are reported in Table 3. Despite the large uncertainties due to the limited sample size, the halo masses of field AGNs inferred from UniverseMachine (M_h) and from the bias measurements (M_{h,b_a}) are consistent within 2σ. We adopt the UniverseMachine estimates as fiducial. We note that, although available only for the field sample, adopting the bias-derived values does not alter the conclusions below.

We compare the M_h of low-luminosity AGNs in our sample with luminous quasars across different cosmic epochs in Figure 8. For the clustering analysis of quasars or AGNs from large-area surveys (e.g., Sloan Digital Sky Survey, Subaru) with reported bias (N. P. Ross et al. 2009; Y. Shen et al. 2009; S. Eftekharzadeh et al. 2015; P. Laurent et al. 2017; J. D. Timlin et al. 2018; J. Arita et al. 2023, 2024), we convert their measured bias values into M_h using our adopted cosmological parameters and the halo bias models of J. L. Tinker et al. (2010) with the COLOSSUS[17] package (B. Diemer 2018). We also present the median halo mass for quasars in A.-C. Eilers et al. (2024), which is derived by searching for analog systems to the quasar fields in UniverseMachine. The bias in J. Arita et al. (2024) from the projected (angular) correlation analysis of 28 low-luminosity broad-line AGNs with photometrically selected galaxies corresponds to $\log(M_h/M_\odot) = 11.5 \pm 0.2$ ($11.4^{+0.2}_{-0.3}$), based on the conversion in this study. These values are consistent with our measurements, accounting for sample variance and systematic uncertainties. In contrast, the host halo masses of luminous quasars at $z = 0$–6 typically exceed $10^{12} M_\odot$, 1–2 dex higher than those of low-luminosity AGNs, while with little dependence on the quasar luminosity (e.g., Y. Shen et al. 2009).

This implies that the differences between low-luminosity AGNs and UV-luminous quasars are not mainly caused by the obscuration from different geometries (H. Netzer 2015). These newly discovered AGNs are not simple counterparts of UV-bright quasars in dust-enshrouded environments. The low-luminosity AGNs discovered by JWST may be inherently distinct from luminous quasars. Instead, they reside in considerably less-massive dark matter halos. Given the comparable halo masses of AGNs and HAEs, along with the high AGN fraction of up to $\gtrsim$17% at $L_{\mathrm{H}\alpha} \approx 10^{43}$ erg s^{-1} (X. Lin et al. 2024), low-luminosity AGNs might represent either a common stage in galaxy evolution or a distinct phase in the BH-galaxy coevolution as discussed in E. Pizzati et al. (2024a).

To explain the characteristics of low-luminosity AGNs, such as their weak X-ray/radio emission and variability, super-Eddington accretion mode has been proposed in many studies (e.g., J. E. Greene et al. 2024; K. Inayoshi et al. 2024; E. Lambrides et al. 2024b; G. Mazzolari et al. 2024). Super-Eddington accretion is also proposed, if these AGNs have low duty cycles ($\lesssim$1%), to reconcile their BH masses (E. Pizzati et al. 2024a). In this case, the predicted host halo masses would be $M_h \sim 10^{11} M_\odot$. Interestingly, this predicted M_h value is consistent with our measurements and M_h derived from an independent simulation suite. Since low-luminosity AGNs and star-forming galaxies occupy halos of comparable mass, the AGN fraction (3.6% in our sample) provides a rough estimate of the duty cycle. This number is broadly consistent with E. Pizzati et al. (2024a).

Multiwavelength observations are essential for better characterizing this population and its accretion mode, including their stellar component, radiation field, and dust content.

[17] https://bdiemer.bitbucket.io/colossus/index.html

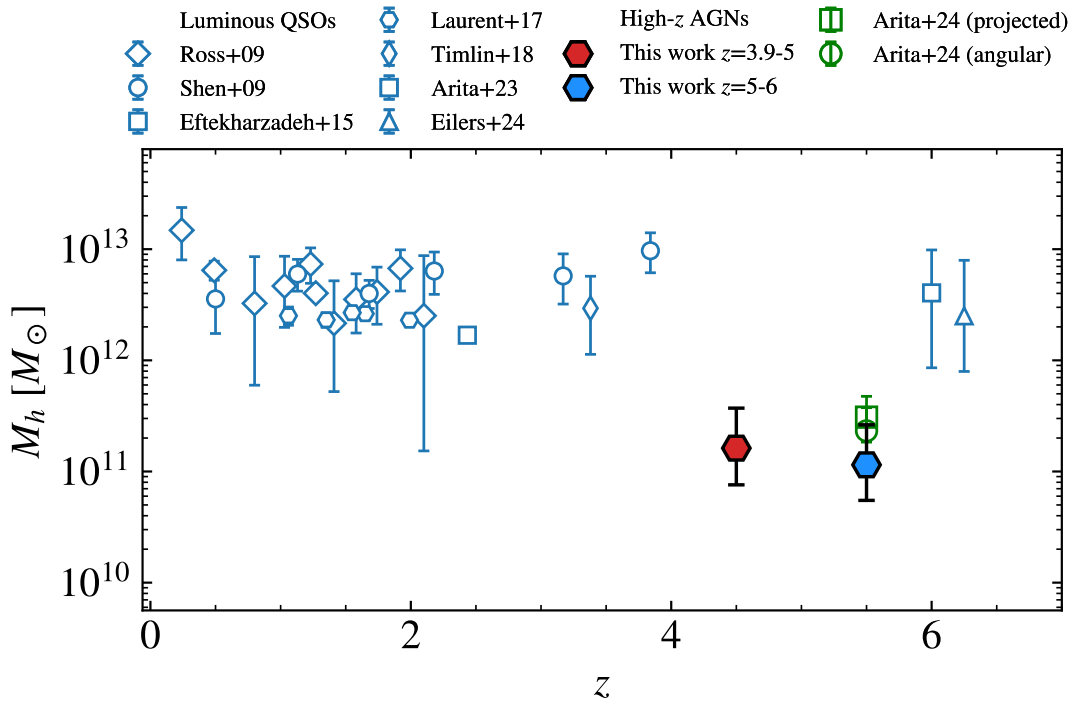

Figure 8. The redshift evolution of dark matter halo masses for quasars and AGNs. For the bias measurements reported in the literature (N. P. Ross et al. 2009; Y. Shen et al. 2009; S. Eftekharzadeh et al. 2015; P. Laurent et al. 2017; J. D. Timlin et al. 2018; J. Arita et al. 2023, 2024), we convert the bias values using our adopted cosmological parameters and the halo bias models from J. L. Tinker et al. (2010). The M_h value from A.-C. Eilers et al. (2024) represents the median halo mass of quasars derived based on UNIVERSEMACHINE. We show two M_h values from J. Arita et al. (2024) in green, derived based on the projected cross-correlation functions of low-luminosity AGNs and photometrically selected galaxies, and their angular cross-correlation, respectively.

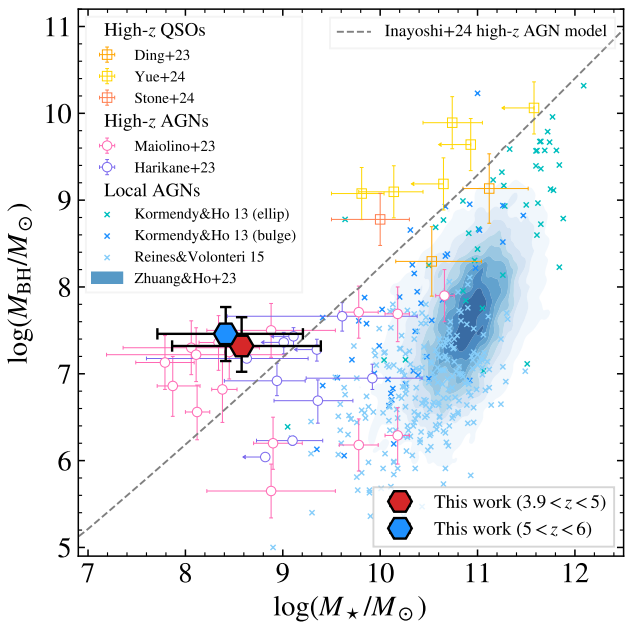

Figure 9. M_{BH}–$M_\star$ relation. The orange and purple hexagons are positioned at the median M_{BH} measured from broad Hα lines, and median $M_\star$ for HAEs at similar redshift. The error bars represent the 16%–84% range. The literature M_{BH} and $M_\star$ values of quasars, high-redshift AGNs, and local AGNs are compiled from J. Kormendy & L. C. Ho (2013), A. E. Reines & M. Volonteri (2015), X. Ding et al. (2023), Y. Harikane et al. (2023), R. Maiolino et al. (2023), M.-Y. Zhuang & L. C. Ho (2023), M. A. Stone et al. (2024), and M. Yue et al. (2024b). The model from K. Inayoshi & K. Ichikawa (2024) is shown as the dashed gray line.

Large-volume surveys are required to probe the multiscale environments of BH growth across a broad range of BH masses.

5.2. Implication for the Host Galaxy Stellar Masses

Assuming the same stellar-to-halo mass ratio distribution, the stellar masses of AGN host galaxies should be also comparable to those of HAEs in the same redshift range. The HAE stellar mass $M_\star$, derived using the UNIVERMACHINE simulations, has a median value of $10^{8.6}M_\odot$ for $3.9 < z < 5$, and $10^{8.4}M_\odot$ for $5 < z < 6$, with 1σ scattering of approximately 0.8 dex in both cases. We note that the $M_\star$ distributions derived here are in good agreement with the $M_\star$ values obtained from the SED fitting.

We adopt the HAEs' $M_\star$ as a proxy for the stellar masses of AGN host galaxies and present the $M_\star$–M_{BH} relation of AGNs in Figure 9. We adopt the M_{BH} values for the grism-selected broad-line AGNs as representatives (Table 1), which range from $10^{6.85}M_\odot$ to $10^{7.99}M_\odot$ at $3.9 < z < 5$ with a median of $10^{7.32}M_\odot$, and from $10^{6.99}M_\odot$ to $10^{8.29}M_\odot$ at $5 < z < 6$ with a median of $10^{7.46}M_\odot$. Our results are consistent with some of the measurements for individual AGNs (R. Maiolino et al. 2023; K. N. Hainline et al. 2024), although the latter exhibit a wide range of $M_\star$ with large uncertainties. On the M_{BH}–$M_\star$ diagram, these high-redshift AGNs have smaller $M_\star$ compared to those of local AGNs with similar M_{BH}. The observed high $M_{BH}/M_\star$ ratio cannot be fully attributed to observational bias (J. Li et al. 2025; Y. Sun et al. 2025). The M_{BH}–$M_\star$ relation for these AGNs is also offset from the theoretical prediction (K. Inayoshi & K. Ichikawa 2024), which was developed to model both high-luminosity quasars and low-luminosity AGNs in the early Universe. These overmassive BHs, with higher $M_{BH}/M_\star$ ratios than predicted values, highlight the need for next-generation models to better understand BH seeding mechanisms and the coevolution of BHs and galaxies.

We also caution that the estimate of M_{BH} is highly uncertain and debated. V. Rusakov et al. (2025) suggested that Balmer

lines may be broadened by electron scattering in regions with high electron column densities. This effect could lead to an overestimation of $M_{\rm BH}$ by 1–2 dex. In contrast, I. Juodžbalis et al. (2025) argued that this claim is untenable. Regardless, the estimates of M_h and the derived $M_\star$ from M_h are independent of $M_{\rm BH}$. If $M_{\rm BH}$ is overestimated, and the true mass is 10^5–$10^7 M_\odot$ as suggested by V. Rusakov et al. (2025), the $M_{\rm BH}$–$M_\star$ relation would better match the model prediction.

6. Summary

In this paper, we study the large-scale environments of low-luminosity AGNs at $3.9 < z < 6$ in the GOODS-North field. By combining the JWST/NIRCam F356W grism from the CONGRESS program and the F444W grism from the FRESCO program, we identify 782 HAEs within this redshift range. From this dataset, we construct a sample of 28 low-luminosity AGNs selected using both the grism and NIRSpec spectra, along with spec-z-confirmed V-shaped SEDs. Our main conclusions are as follows:

1. Low-luminosity AGNs reside in a diverse range of large-scale environments. These AGNs are found in regions with overdensity fields δ within 15 cMpc spanning from low densities of $\delta = -0.56$ to high densities of $\delta = 10.56$. Notably, five AGNs are located in a protocluster at $z = 4.41$ and seven AGNs lie in filamentary structures at $z \approx 5.19$. Among the 28 AGNs, 10 ($36\% \pm 9\%$) are located in regions with overdensity $\delta > 3$, a fraction consistent with that of HAEs in $\delta > 3$ regions ($30\% \pm 2\%$). This implies that AGNs do not preferentially reside in denser environments compared to HAEs.
2. No clear correlations are found between the overdensity field (δ; within $15\,h^{-1}$ cMpc of AGNs) and their broad Hα luminosities, broad Hα FWHMs, or BH masses. The AGN fraction among star-forming galaxies also shows no dependence on δ. These results suggest that large-scale environments (>10 cMpc) may not significantly influence BH growth and AGN evolution on smaller (pc) scales.
3. The projected surface density excess of AGNs is consistent with that of HAEs, indicating that star-forming galaxies do not cluster more strongly around AGNs. This qualitatively indicates that the dark matter halos of AGNs have masses similar to those of star-forming galaxies.
4. The cross-correlations between AGNs and HAEs exhibit an amplitude comparable to that of the HAE autocorrelations at both $3.9 < z < 5$ and $5 < z < 6$. When considering AGNs and HAEs in the fields alone, the correlation length of the AGN-HAE cross-correlation is $4.26^{+0.70}_{-0.61}\,h^{-1}$ cMpc with a power-law index $\gamma = 1.59$ at $3.9 < z < 5$, and $7.66^{+0.90}_{-0.81}\,h^{-1}$ cMpc with $\gamma = 1.63$ at $5 < z < 6$. These values are consistent with those of the HAE autocorrelations within 1σ. It suggests that AGNs and HAEs share similar bias parameters ($b_a \approx b_g$) and, consequently, reside in dark matter halos of comparable mass.
5. Adopting the halo mass distribution for HAEs derived using the UniverseMachine simulation (X. Lin et al. 2025), we find that low-luminosity AGNs are hosted by dark matter halos with masses of $\log(M_h/M_\odot)$=11.0–11.2, with 1σ scattering of 0.3–0.4 dex. Their M_h values are 1–2 dex lower than those of luminous quasars at similar redshifts. The less-biased host dark matter halos suggest that low-luminosity AGNs likely represent a distinct evolutionary phase or AGN population. Interestingly, our $M_h \approx 10^{11} M_\odot$ estimate is consistent with the low-duty cycle scenarios required for super-Eddington accretion, as suggested in simulations (E. Pizzati et al. 2024a).
6. Assuming the same stellar-to-halo mass ratio for AGNs and HAEs, the stellar masses ($M_\star$) of AGN host galaxies are $\log(M_\star/M_\odot) = 8.2$–$8.4$ with a typical 1σ scattering of 0.8 dex. The low-luminosity AGNs have overmassive BHs, showing higher $M_\star/M_{\rm BH}$ ratios compared to local type-1 AGNs and theoretical predictions (K. Inayoshi & K. Ichikawa 2024).

To better understand the nature of the JWST-selected low-luminosity AGNs, deep, wider spectroscopic surveys with large AGN samples across a wide range of BH masses and luminosity ranges are required. Deep spectroscopic surveys with large AGN samples, such as SAPPHIRES (GO 6434, PI Egami; F. Sun et al. 2025), will bring insights into the impact of local conditions on BH growth by small-scale clustering analysis. Wide grism surveys, like COSMOS-3D (GO 5893; PI Kakiichi) and NEXUS (GO 5105; PI Shen, Y. Shen et al. 2024), will provide better constraints on the halo masses across different luminosities, while also helping to mitigate cosmic variance.

Acknowledgments

We thank the anonymous referee for providing constructive comments. We thank Nickolas Kokron, Michael Strauss, and Yin Li for very helpful discussions on the clustering analysis. X.L. and X.F. acknowledge support from the NSF award AST-2308258. F.W. acknowledges support from NSF award AST-2513040. X.L. and Z.C. acknowledge support from the National Key R&D Program of China (grant No. 2023YFA1605600) and Tsinghua University Initiative Scientific Research Program (No. 20223080023). A.J.B. acknowledges funding from the "First-Galaxies" Advanced Grant from the European Research Council (ERC) under the European Union's Horizon 2020 research and innovation program (grant agreement No. 789056). B.E.R. acknowledges support from the NIRCam Science Team contract to the University of Arizona, NAS5-02015, and JWST Program 3215. S.T. acknowledges support by the Royal Society Research grant G125142. C.N.A.W. acknowledges JWST/NIRCam contract to the University of Arizona NAS5-02015. R.M. acknowledges support by the Science and Technology Facilities Council (STFC), by the ERC through Advanced grant 695671 "QUENCH," and by the UKRI Frontier Research grant RISE and FALL. R.M. also acknowledges funding from a research professorship from the Royal Society.

This work is based on observations made with the NASA/ESA Hubble Space Telescope and NASA/ESA/CSA James Webb Space Telescope. The data were obtained from the Mikulski Archive for Space Telescopes at the Space Telescope Science Institute, which is operated by the Association of Universities for Research in Astronomy, Inc., under NASA contract NAS 5-03127 for JWST. These observations are associated with program Nos. 1181 (JADES), 1895 (FRESCO), and 3577 (CONGRESS). Support for program No. 3577 was provided by NASA through a grant from the Space Telescope Science Institute, which is operated by the Association of

Universities for Research in Astronomy, Inc., under NASA contract NAS 5-03127. The authors acknowledge the FRESCO team for developing their observing program with a zero-exclusive-access period.

Data Availability

The JWST data presented in this article were obtained from the Mikulski Archive for Space Telescopes (MAST) at the Space Telescope Science Institute. The data of the FRESCO survey (The FRESCO Collaboration 2023) is available at doi:10.17909/gdyc-7g80; the data of the CONGRESS survey is available at doi:10.17909/6rfk-6s81; the data of the JADES survey (The JADES Collaboration 2023) is available at doi:10.17909/8tdj-8n28.

Appendix
AGN sample

We show the NIRCam images of our grism-selected AGN sample in Figure A1, NIRSpec-selected sample in Figure A2, and V-shaped-selected sample in Figure A3. For the V-shaped-selected sample, we present their rest-frame SEDs in Figure A4, which clearly exhibit bluer UV continuum slopes than the optical continuum slopes.

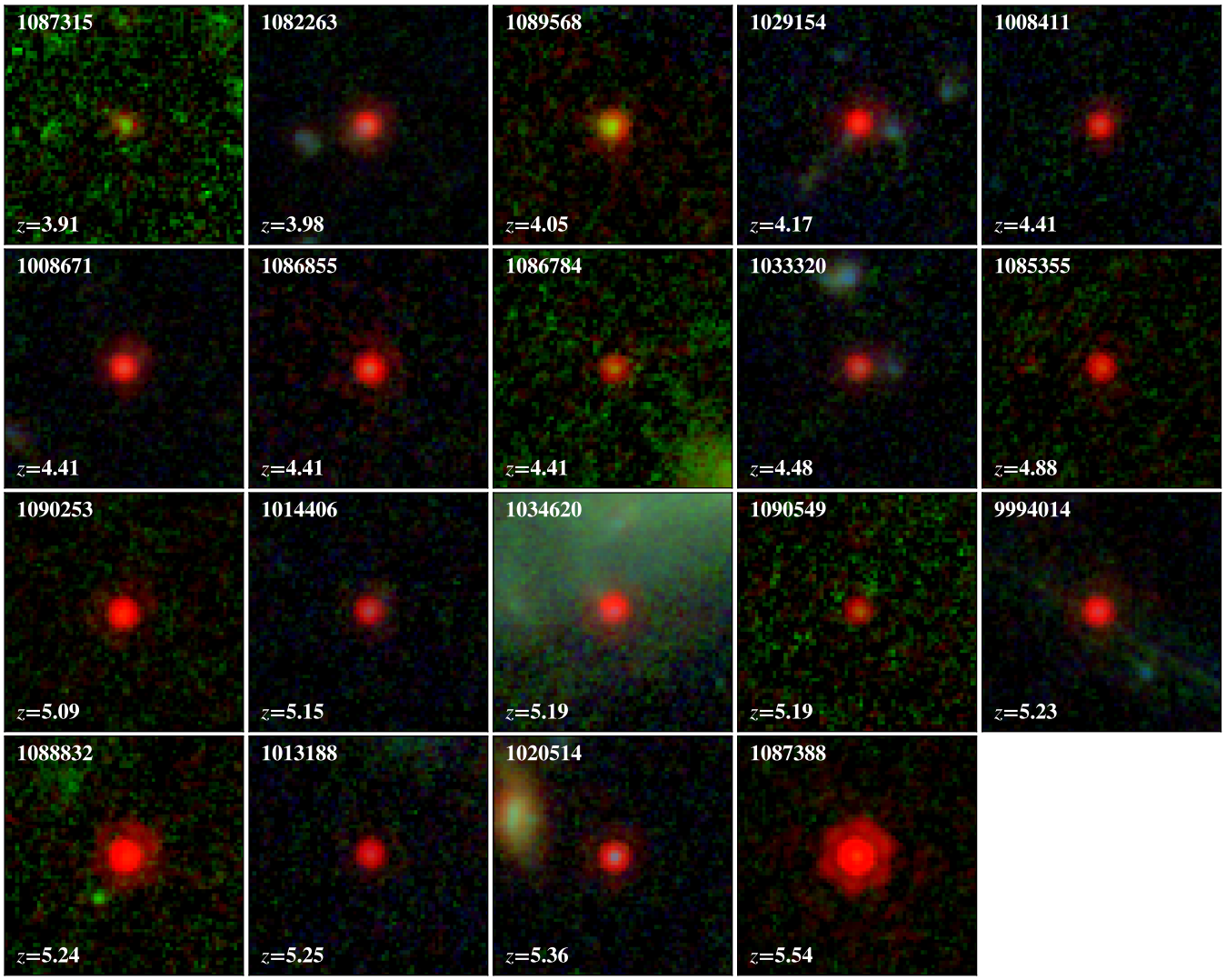

Figure A1. The 19 AGNs in the sample, identified through their broad Hα emission lines from JWST/NIRCam WFSS. For each AGN, we present a $2'' \times 2''$ thumbnail composed of F356W (or F444W for $z > 5$), F200W, and F115W images. For the sources 1085355, 1086784, 1087315, 1087388, 1088832, 1089568, 1090253, and 1090549, F210M images are used in place of F200W.

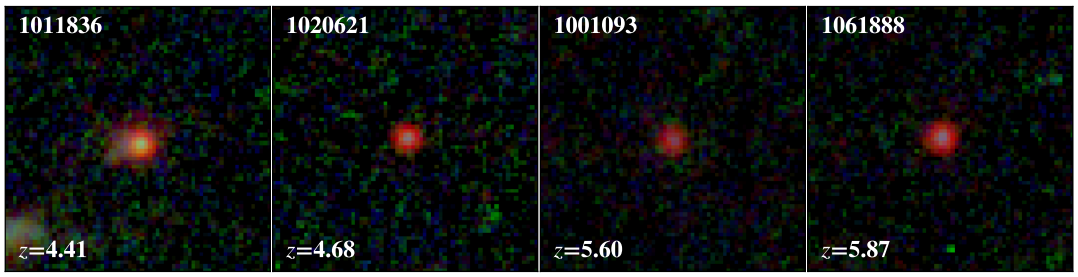

Figure A2. Similar to Figure A1 but for the four AGNs in the sample identified through their broad Hα emission lines from JWST/NIRSpec Grating R1000 spectra (R. Maiolino et al. 2023).

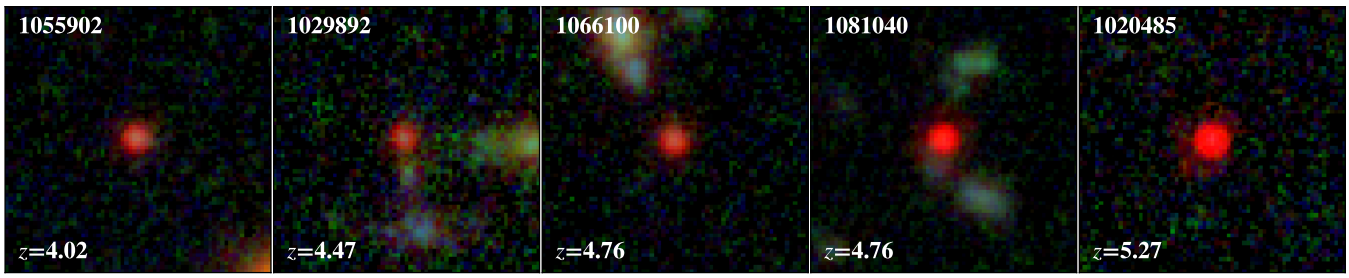

Figure A3. Similar to Figure A1 but for the five AGNs in the sample identified through their V-shaped SEDs.

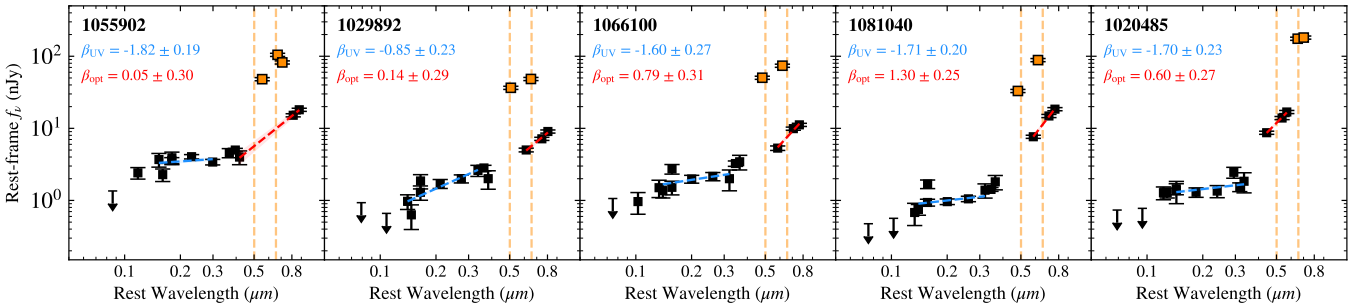

Figure A4. The rest-frame SEDs of the five V-shaped-selected AGNs. All of the photometry shown is measured with Kron radii of 1.2. The continuum photometry is represented by black squares, while the bands containing emission lines (Hβ, [O III] $\lambda\lambda$4960,5008, and Hα) are marked as orange squares. The wavelengths of the emission lines are indicated by dashed orange vertical lines. The blue and red dashed lines represent the best-fit power-law models to the UV and optical continuum SEDs, respectively, with the corresponding shaded regions indicating the 1σ uncertainty.

ORCID iDs

Xiaojing Lin https://orcid.org/0000-0001-6052-4234
Xiaohui Fan https://orcid.org/0000-0003-3310-0131
Fengwu Sun https://orcid.org/0000-0002-4622-6617
Junyu Zhang https://orcid.org/0000-0002-1574-2045
Eiichi Egami https://orcid.org/0000-0003-1344-9475
Jakob M. Helton https://orcid.org/0000-0003-4337-6211
Feige Wang https://orcid.org/0000-0002-7633-431X
Haowen Zhang https://orcid.org/0000-0002-4321-3538
Andrew J. Bunker https://orcid.org/0000-0002-8651-9879
Zheng Cai https://orcid.org/0000-0001-8467-6478
Zhiyuan Ji https://orcid.org/0000-0001-7673-2257
Xiangyu Jin https://orcid.org/0000-0002-5768-738X
Roberto Maiolino https://orcid.org/0000-0002-4985-3819
Maria Anne Pudoka https://orcid.org/0000-0003-4924-5941
Pierluigi Rinaldi https://orcid.org/0000-0002-5104-8245
Brant Robertson https://orcid.org/0000-0002-4271-0364
Sandro Tacchella https://orcid.org/0000-0002-8224-4505
Wei Leong Tee https://orcid.org/0000-0003-0747-1780
Yang Sun https://orcid.org/0000-0001-6561-9443
Christopher N. A. Willmer https://orcid.org/0000-0001-9262-9997
Chris Willott https://orcid.org/0000-0002-4201-7367
Yongda Zhu https://orcid.org/0000-0003-3307-7525

References

Akins, H. B., Casey, C. M., Lambrides, E., et al. 2025, ApJ, 991, 37
Arita, J., Kashikawa, N., Matsuoka, Y., et al. 2023, ApJ, 954, 210
Arita, J., Kashikawa, N., Onoue, M., et al. 2025, MNRAS, 536, 3677
Bañados, E., Venemans, B. P., Mazzucchelli, C., et al. 2018, Natur, 553, 473
Baggen, J. F. W., van Dokkum, P., Brammer, G., et al. 2024, ApJL, 977, L13
Behroozi, P., Wechsler, R. H., Hearin, A. P., & Conroy, C. 2019, MNRAS, 488, 3143
Brammer, G. B., van Dokkum, P. G., & Coppi, P. 2008, ApJ, 686, 1503
Cai, Z., Fan, X., Peirani, S., et al. 2016, ApJ, 833, 135
Cammelli, V., Monaco, P., Tan, J. C., et al. 2025, MNRAS, 536, 851
Casey, C. M., Akins, H. B., Kokorev, V., et al. 2024, ApJL, 975, L4
Chen, H., Eilers, A.-C., Bosman, S. E. I., et al. 2022, ApJ, 931, 29
Chiang, Y.-K., Overzier, R., & Gebhardt, K. 2013, ApJ, 779, 127
Chiang, Y.-K., Overzier, R., & Gebhardt, K. 2014, ApJL, 782, L3
Comastri, A., Gilli, R., Marconi, A., Risaliti, G., & Salvati, M. 2015, A&A, 574, L10
Cucciati, O., Zamorani, G., Lemaux, B. C., et al. 2014, A&A, 570, A16

Curran, P. A. 2014, arXiv:1411.3816
Davies, F. B., Hennawi, J. F., & Eilers, A.-C. 2019, ApJL, 884, L19
Davies, F. B., Hennawi, J. F., & Eilers, A.-C. 2020, MNRAS, 493, 1330
Desjacques, V., Jeong, D., & Schmidt, F. 2018, PhR, 733, 1
D'Eugenio, F., Cameron, A. J., Scholtz, J., et al. 2025, ApJS, 277, 4
Diemer, B. 2018, ApJS, 239, 35
Ding, X., Onoue, M., Silverman, J. D., et al. 2023, Natur, 621, 51
Eftekharzadeh, S., Myers, A. D., White, M., et al. 2015, MNRAS, 453, 2779
Eilers, A.-C., Davies, F. B., Hennawi, J. F., et al. 2017, ApJ, 840, 24
Eilers, A.-C., Hennawi, J. F., Decarli, R., et al. 2020, ApJ, 900, 37
Eilers, A.-C., Mackenzie, R., Pizzati, E., et al. 2024, ApJ, 974, 275
Eisenstein, D. J., Willott, C., Alberts, S., et al. 2023, arXiv:2306.02465
Fan, X., Bañados, E., & Simcoe, R. A. 2023, ARA&A, 61, 373
Farina, E. P., Schindler, J.-T., Walter, F., et al. 2022, ApJ, 941, 106
Gardner, J. P., Mather, J. C., Abbott, R., et al. 2023, PASP, 135, 068001
Greene, J. E., & Ho, L. C. 2005, ApJ, 630, 122
Greene, J. E., Labbe, I., Goulding, A. D., et al. 2024, ApJ, 964, 39
Geach, J. E., Sobral, D., Hickox, R. C., et al. 2012, MNRAS, 426, 679
Greene, T. P., Chu, L., Egami, E., et al. 2016, SPIE, 9904, 99040E
Hainline, K. N., Johnson, B. D., Robertson, B., et al. 2024, ApJ, 964, 71
Harikane, Y., Ouchi, M., Ono, Y., et al. 2016, ApJ, 821, 123
Harikane, Y., Zhang, Y., Nakajima, K., et al. 2023, ApJ, 959, 39
Helton, J. M., Sun, F., Woodrum, C., et al. 2024, ApJ, 974, 41
Hennawi, J. F., Kist, T., Davies, F. B., & Tamanas, J. 2025, MNRAS, 539, 2621
Hennawi, J. F., Strauss, M. A., Oguri, M., et al. 2006, AJ, 131, 1
Herard-Demanche, T., Bouwens, R. J., Oesch, P. A., et al. 2025, MNRAS, 537, 788
Herrero Alonso, Y., Miyaji, T., Wisotzki, L., et al. 2023, A&A, 671, A5
Horne, K. 1986, PASP, 98, 609
Illingworth, G. 2017, HST Proposal, id.15027. Cycle 25
Inayoshi, K., & Ichikawa, K. 2024, ApJL, 973, L49
Inayoshi, K., Kimura, S., & Noda, H. 2025, PASJ, 77, 811
Inayoshi, K., Nakatani, R., Toyouchi, D., et al. 2022, ApJ, 927, 237
Juodžbalis, I., Maiolino, R., Baker, W. M., et al. 2025, arXiv:2504.03551
Kokorev, V., Caputi, K. I., Greene, J. E., et al. 2024, ApJ, 968, 38
Kokubo, M., & Harikane, Y. 2025, ApJ, 995, 24
Kormendy, J., & Ho, L. C. 2013, ARA&A, 51, 511
Lambrides, E., Chiaberge, M., Long, A. S., et al. 2024a, ApJL, 961, L25
Lambrides, E., Garofali, K., Larson, R., et al. 2024b, arXiv:2409.13047
Landy, S. D., & Szalay, A. S. 1993, ApJ, 412, 64
Laurent, P., Eftekharzadeh, S., Le Goff, J.-M., et al. 2017, JCAP, 2017, 017
Leung, G. C. K., Finkelstein, S. L., Pérez-González, P. G., et al. 2025, ApJ, 992, 26
Lewis, A., & Challinor, A., 2011 CAMB: Code for Anisotropies in the Microwave Background, Astrophysics Source Code Library, ascl:1102.026
Li, J., Silverman, J. D., Shen, Y., et al. 2025, ApJ, 981, 19
Li, Z., Inayoshi, K., Chen, K., Ichikawa, K., & Ho, L. C. 2025, ApJ, 980, 36
Lim, S., Tacchella, S., Schaye, J., et al. 2024, MNRAS, 532, 4551
Lin, X., Egami, E., Sun, F., et al. 2025, arXiv:2504.08028
Lin, X., Wang, F., Fan, X., et al. 2024, ApJ, 974, 147
Lyu, J., Alberts, S., Rieke, G. H., et al. 2024, ApJ, 966, 229
Ma, Y., Greene, J. E., Setton, D. J., et al. 2025, ApJ, 981, 191
Maiolino, R., Risaliti, G., Signorini, M., et al. 2025, MNRAS, 538, 1921
Maiolino, R., Scholtz, J., Curtis-Lake, E., et al. 2024, A&A, 691, A145
Matthee, J., Mackenzie, R., Simcoe, R. A., et al. 2023, ApJ, 950, 67
Matthee, J., Naidu, R. P., Brammer, G., et al. 2024, ApJ, 963, 129
Matthee, J., Naidu, R. P., Kotiwale, G., et al. 2025, ApJ, 988, 246
Mazzolari, G., Gilli, R., Maiolino, R., et al. 2024, arXiv:2412.04224
Netzer, H. 2015, ARA&A, 53, 365
Ni, Y., Di Matteo, T., Gilli, R., et al. 2020, MNRAS, 495, 2135
Oesch, P. A., Brammer, G., Naidu, R. P., et al. 2023, MNRAS, 525, 2864
Pérez-González, P. G., Barro, G., Rieke, G. H., et al. 2024, ApJ, 968, 4
Pizzati, E., Hennawi, J. F., Schaye, J., et al. 2025, MNRAS, 539, 2910
Pizzati, E., Hennawi, J. F., Schaye, J., et al. 2024, MNRAS, 534, 3155
Privon, G. C., Ricci, C., Aalto, S., et al. 2020, ApJ, 893, 149
Pudoka, M., Wang, F., Fan, X., et al. 2024, ApJ, 968, 118
Puskás, D., Tacchella, S., Simmonds, C., et al. 2025, MNRAS, 540, 2146
Regan, J., & Volonteri, M. 2024, OJAp, 7, 72
Reines, A. E., & Volonteri, M. 2015, ApJ, 813, 82
Rieke, M. J., Robertson, B., Tacchella, S., et al. 2023, ApJS, 269, 16
Rinaldi, P., Bonaventura, N., Rieke, G. H., et al. 2025, ApJ, 992, 71
Robertson, B., Johnson, B. D., Tacchella, S., et al. 2024, ApJ, 970, 31
Ross, N. P., Shen, Y., Strauss, M. A., et al. 2009, ApJ, 697, 1634
Rusakov, V., Watson, D., Nikopoulos, G. P., et al. 2025, arXiv:2503.16595
Schindler, J.-T., Hennawi, J. F., Davies, F. B., et al. 2025, NatAs, 9, 1732
Shen, Y., Strauss, M. A., Ross, N. P., et al. 2009, ApJ, 697, 1656
Shen, Y., Zhuang, M.-Y., Li, J., et al. 2024, arXiv:2408.12713
Stone, M. A., Lyu, J., Rieke, G. H., Alberts, S., & Hainline, K. N. 2024, ApJ, 964, 90
Sun, F., Egami, E., Pirzkal, N., et al. 2022, ApJL, 936, L8
Sun, F., Egami, E., Pirzkal, N., et al. 2023, ApJ, 953, 53
Sun, F., Helton, J. M., Egami, E., et al. 2024, ApJ, 961, 69
Sun, F., Fudamoto, Y., Lin, X., et al. 2025, arXiv:2503.15587
Sun, Y., Rieke, G. H., Lyu, J., et al. 2025, arXiv:2503.03675
Tee, W. L., Fan, X., Wang, F., & Yang, J. 2025, ApJL, 983, L26
The FRESCO Collaboration 2023, FRESCO: MAST High Level Science Product, MAST High Level Science Product, Mikulski Archive for Space Telescopes (MAST), STScI/MAST, doi:10.17909/gdyc-7g80
The JADES Collaboration 2023, JWST Advanced Deep Extragalactic Survey (JADES): MAST High Level Science Product, MAST High Level Science Product, Mikulski Archive for Space Telescopes (MAST), STScI/MAST, doi:10.17909/8tdj-8n28
Timlin, J. D., Ross, N. P., Richards, G. T., et al. 2018, ApJ, 859, 20
Tinker, J. L., Robertson, B. E., Kravtsov, A. V., et al. 2010, ApJ, 724, 878
Trakhtenbrot, B., Netzer, H., Lira, P., & Shemmer, O. 2011, ApJ, 730, 7
Trinca, A., Valiante, R., Schneider, R., et al. 2024, arXiv:2412.14248
Wang, B., Leja, J., de Graaff, A., et al. 2024, ApJL, 969, L13
Wang, F., Yang, J., Fan, X., et al. 2021, ApJL, 907, L1
Williams, C. C., Alberts, S., Ji, Z., et al. 2024, ApJ, 968, 34
Yang, J., Wang, F., Fan, X., et al. 2020, ApJL, 897, L14
Yang, J., Wang, F., Fan, X., et al. 2021, ApJ, 923, 262
Yue, M., Eilers, A.-C., Ananna, T. T., et al. 2024a, ApJL, 974, L26
Yue, M., Eilers, A.-C., Simcoe, R. A., et al. 2024b, ApJ, 966, 176
Zhang, J., Egami, E., Sun, F., et al. 2025, arXiv:2505.02895
Zhang, Z., Jiang, L., Liu, W., & Ho, L. C. 2025, ApJ, 985, 119
Zhuang, M.-Y., & Ho, L. C. 2023, NatAs, 7, 1376